Gondwana Research 22 (2012) 360–376

Contents lists available at SciVerse ScienceDirect

Gondwana Research

journal homepage: www.elsevier.com/locate/gr

The Himalayan leucogranites: Constraints on the nature of their crustal source region and geodynamic setting

Zhengfu Guo [a,*], Marjorie Wilson [b]

[a] Key Laboratory of Cenozoic Geology and Environment, Institute of Geology and Geophysics, Chinese Academy of Sciences, P.O. Box 9825, Beijing 100029, China
[b] School of Earth and Environment, University of Leeds, Leeds LS2 9JT, UK

ARTICLE INFO

Article history:
Received 10 February 2011
Received in revised form 18 July 2011
Accepted 25 July 2011
Available online 11 August 2011

Keywords:
Leucogranites
Decompression melting
Himalayan orogen
Steepening of the subducted Indian slab

ABSTRACT

Late Oligocene–Miocene leucogranites within southern Tibet form part of an extensive intrusive igneous province within the Himalayan orogen. The main rock types are tourmaline leucogranites (Tg) and two-mica leucogranites (2 mg). They have high SiO_2 (70.56–75.32 wt.%), Al_2O_3 (13.55–15.67 wt.%) and $(^{87}Sr/^{86}Sr)_i$ (0.724001–0.797297), and low MgO (0.02–0.46 wt.%) and $(^{143}Nd/^{144}Nd)_i$ (0.511693–0.511906). Chondrite-normalized rare earth element (REE) patterns display strong negative Eu anomalies. Whole-rock major and trace element and Sr–Nd isotope data for the leucogranites suggest that their source region was a two-component mixture between a fluid derived from the Lesser Himalayan (LH) crustal sequence and the bulk crust of the Higher Himalayan (HH) sequence. Trace element and Sr–Nd isotope modeling indicate that the proportion of fluid derived from the LH sequence varied from 2% to 19% and the resulting metasomatised source experienced 7–16% melting. The amount of fluid derived from the LH sequence increases from north to south. Northward underthrusting of the Indian continent resulted in infiltration of the LH-derived fluid into the overlying HH sequence. Subsequent decompression melting of this metasomatised crust, mostly during the Miocene (25–9 Ma), generated the leucogranites. This may be linked to steepening of the subducted slab of Indian lithosphere beneath the orogenic belt.

1. Introduction

Late Oligocene–Miocene leucogranite bodies in southern Tibet form part of an E–W-striking, ~3000 km long igneous intrusive province in the Himalayan orogen (Fig. 1). These Himalayan leucogranites potentially provide an important tool to constrain the tectono-magmatic history of the orogen (Zhang et al., 2004, 2005; Yin, 2006; King et al., 2011); however, their geodynamic setting remains a subject for debate. Although there have been numerous studies of the leucogranites (e.g. Harrison et al., 1999; Visona and Lombardo, 2002; Searle et al., 2003; Zhang et al., 2004, 2005; King et al., 2011), their source region and petrogenesis remain highly controversial. The main arguments focus on two aspects: (1) What is the source composition of the Himalayan leucogranites? Some workers (e.g. Le Fort et al., 1987; Visona and Lombardo, 2002) have suggested that this involved two-component mixing between the Lesser Himalayan (LH) and Higher Himalayan (HH) sequences, whereas other workers (e.g. Harris and Massey, 1994; Guillot and Le Fort, 1995; Harrison et al., 1999; Zhang et al., 2004) proposed that the leucogranites resulted from melting of the HH sequence only. (2) What is the most likely petrogenetic model for the Himalayan leucogranites? This has been variously attributed to (a) fluid-present melting (e.g. Le Fort et al., 1987; Harris et al., 1993; Patino Douce and Harris, 1998), (b) decompression melting (e.g. Harris and Massey, 1994; Davidson et al., 1997) and (c) over-heating melting (e.g. Bird, 1978; Harrison et al., 1999; Visona and Lombardo, 2002). However, there is little geophysical evidence to support the over-heating melting model (e.g. Nelson et al., 1996). The lack of detailed sampling and of petrological and geochemical data has precluded further constraints on the source region and petrogenesis of the Himalayan leucogranites.

This study reports new geochemical and Sr–Nd isotope data for six leucogranite bodies from the Himalayas (Fig. 1). Whole-rock major and trace element and Sr–Nd isotope data are used to define the characteristics of the leucogranite bodies studied. These data complement those of previous studies (e.g. Harrison et al., 1997; Searle and Godin, 2003) that predominantly focused on the leucogranites of Nepal and Bhutan, and the most recent work of King et al. (2011) on the Sakya dome of southern Tibet. Based on the new data presented and previously published data, we explore the source region composition and petrogenesis of the Himalayan leucogranites.

2. Geological background

The Himalayan orogen is defined by the Indus-Tsangpo Suture (ITS) to the north and the Main Frontal Thrust (MFT) to the south (Fig. 1). From north to south the orogen comprises four roughly parallel, laterally continuous tectonostratigraphic units (e.g. Godin et al., 2001; Yin, 2006): (1) the Tethyan Himalayan (TH) sequence,

* Corresponding author. Tel.: +86 10 82998393; fax: +86 10 62010846.
E-mail address: zfguo@mail.iggcas.ac.cn (Z. Guo).

1342-937X/$ – see front matter
doi:10.1016/j.gr.2011.07.027

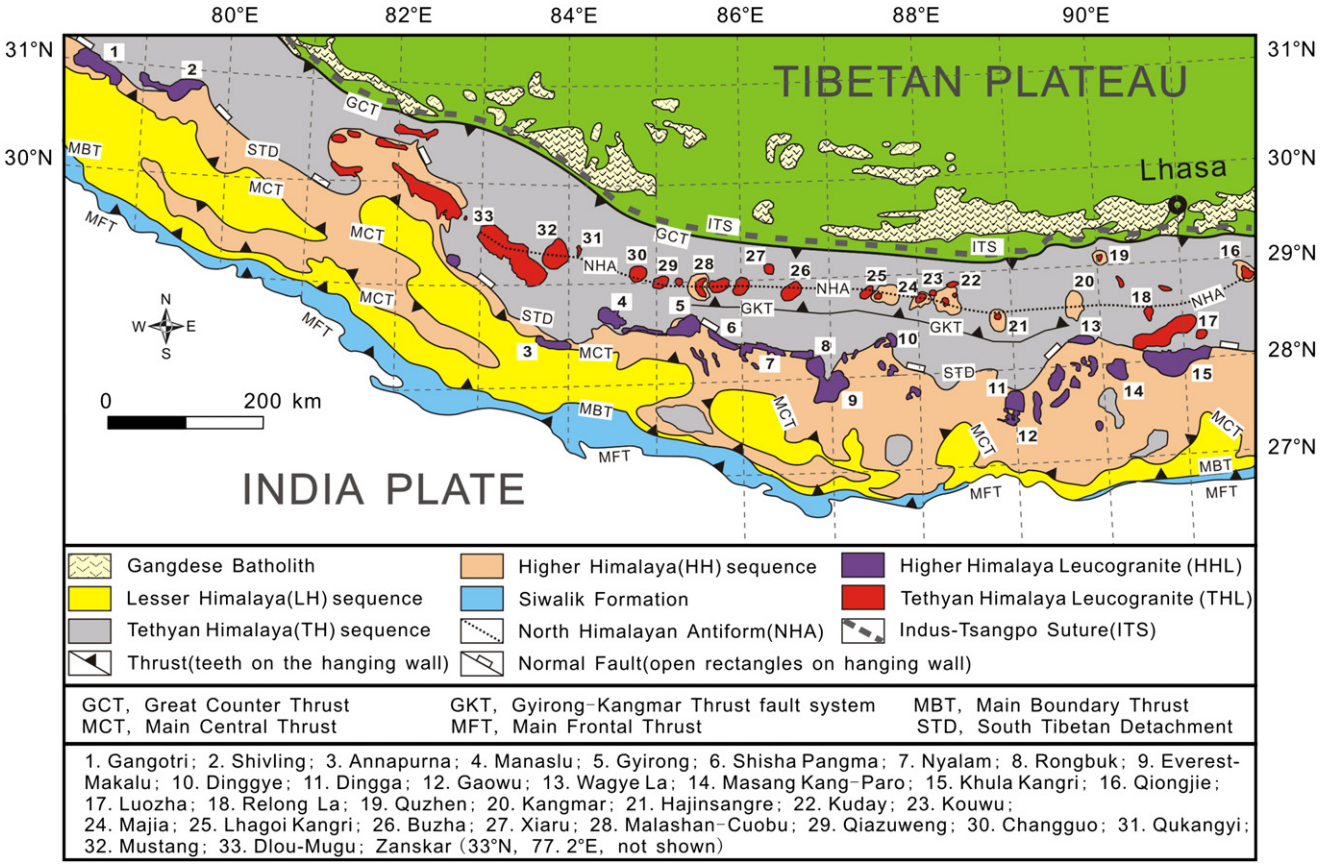

Fig. 1. Simplified map showing the distribution of leucogranites in the Himalayas (Modified from Harrison et al., 1999; Searle et al., 2003; Pan and Ding, 2004; Aoya et al., 2005; Yin, 2006). Abbreviations as follows: HH, Higher Himalayan Crystalline; LH, Lesser Himalayan Sequence; TH, Tethyan Himalayan Sequence; HHL, Higher Himalayan leucogranite; THL, Tethyan Himalayan leucogranite. Leucogranite bodies studied here are Numbers. 5, 7, 10, 12, 17 and 19.

composed of Proterozoic to Eocene siliciclastic and carbonate sedimentary and volcanic rocks; (2) the Higher Himalayan (HH) sequence, composed of Paleoproterozoic to Ordovician high-grade metamorphic rocks; (3) the Lesser Himalayan (LH) sequence, composed of Proterozoic–Cambrian low-grade metasedimentary rocks (Richards et al., 2005); and (4) the Neogene Siwalik Formation (Fig. 1). Previous studies (e.g. Guillot et al., 1994; Godin et al., 2001; Yin, 2006 and references therein) have identified three north-dipping tectonic boundaries between the tectonostratigraphic units from north to south (Fig. 1): (1) the South Tibetan Detachment (STD) system, which is a late Oligocene to Miocene (25–12 Ma) normal fault juxtaposing the TH sequence in the hanging wall against the HH sequence in the footwall; (2) the Main Central Thrust (MCT), which is interpreted as a shear zone along which the HH sequence was emplaced southward over the LH sequence; and (3) the Main Boundary Thrust (MBT), which is defined as a thrust placing the LH sequence over the Neogene Siwalik Formation (Fig. 1). The INDEPTH seismic reflection data of Nelson et al. (1996) indicate that the major Himalayan thrusts (MCT, MBT and MFT) sole into the low-angle Main Himalayan Thrust (MHT) beneath the TH sequence.

The Himalayan leucogranites comprise two roughly parallel, near E–W striking, intrusive belts; from north to south these are (Fig. 1): (1) the Tethyan Himalayan leucogranites (THL) and (2) the Higher Himalayan leucogranites (HHL) belts. King et al. (2011) refer to the THL as “North Himalayan granites”, but we do not adopt this terminology here. The THL are located in the axial zone of the North Himalayan Antiform (NHA) within the TH sequence, whereas the HHL are located within the HH sequence (Zhang et al., 2004, 2005). The NHA exposes a discontinuous series of gneiss domes, comprising Palaeozoic granite gneisses and Neoproterozoic to early Palaeozoic high grade metasediments, including migmatites (King et al., 2011); these represent tectonic windows into the underlying HH crustal sequence. The THL intrude both the gneiss domes and the overlying Tethyan sedimentary series (Fig. 1). The ages of the Himalayan leucogranites range from ca 9 to 25 Ma (Table 1).

Six leucogranite bodies from the Himalayas form the basis of this study; they are located in both the HHL (Gyirong, Nyalam, Dinggye and Gaowu) and the THL (Luozha and Quzhen) belts from south to north (Fig. 1 and Table 1). The leucogranite bodies analyzed (Fig. 1 and Table 1) include both plutons and dykes. The Gyirong, Nyalam, Dinggye, Gaowu and Quzhen samples are from plutons whereas those from Luozha include both plutons and dykes. In general, the exposed areas of the plutons are relatively small, ranging from 5 km^2 to 50 km^2. They intrude pre-Cambrian and Palaeozoic–Mesozoic gneisses and metasediments in the TH and HH sequences (Fig. 1).

3. Petrography

The leucogranites studied are ubiquitously leucocratic without mafic enclaves and have a relatively uniform mineralogy. To estimate their modal mineralogy, three perpendicular thin sections were cut for each sample. The main minerals include plagioclase, potassic feldspar (K-feldspar), biotite, muscovite, tourmaline and quartz; the accessory minerals are dominated by garnet, apatite, zircon, monazite and magnetite (Table 2). Plagioclase is euhedral to subhedral with weak zoning. Perthitic K-feldspar is subhedral to anhedral. Euhedral to subhedral biotite mostly grows together with muscovite, which is often euhedral. Tourmaline is euhedral to subhedral, and displays

progressive zoning with blue cores and brown rims. Quartz occurs as rounded grains.

Following previous studies of the Himalayan leucogranites (e.g., Guillot and Le Fort, 1995; Visona and Lombardo, 2002), the leucogranites have been sub-divided into two types based on their modal contents of biotite, muscovite and tourmaline (Table 2): (1) tourmaline leucogranites (Tg) and (2) two-mica leucogranites (2 mg). The Tg have abundant tourmaline and muscovite, and scarce biotite, whereas the 2 mg are composed of abundant biotite and muscovite, and are devoid of tourmaline. The 2 mg are mainly fine- to medium-grained whereas the Tg are medium-to coarse-grained. The Tg are dominantly exposed in the HH sequence, whereas the 2 mg are intruded within both the HH and TH sequence (Fig. 1).

Table 1
Ages of the Himalayan leucogranites.

Body no.	Body name	Mineral dated	Method	Age (Ma)	Data sources
1	Gangotri	Monazite	U–Pb	22.4	(1)
2	Shivling	Monazite	U–Pb	23.0; 21.9	(1, 2)
3	Annapurna	Zircon	U–Pb	22.1	(3)
4	Manaslu	Monazite	U–Pb	22.9; 19.3; 22.4; 19.0; 25.0; 18.1; 25.7; 24.9; 13–21.4	(1, 4, 5, 6)
		Muscovite, biotite, hornblende	Ar–Ar	17.6–24.4	(7)
5	Gyirong	Monazite	U–Pb	16.1	(8)
6	Shisha Pangma	Monazite	U–Pb	20.2; 17.3	(9)
7	Nyalam	Monazite	U–Pb	16.8	(10)
8	Rongbuk	Monazite	U–Pb	20.3; 22.0; 16.8; 16.4; 16.2	(2, 5, 11)
9	Everest–Makalu	Monazite	U–Pb	20.5; 21.3; 21.9; 24.0; 23.0	(2, 4, 12)
		Zircon	U–Pb	23.8; 23.2	(13)
		Monazite and zircon	U–Pb	14.3	(10)
10	Dinggye	Monazite	U–Pb	15	(14)
11	Dingga	Muscovite	Ar–Ar	14.9; 15.3	(8)
12	Gaowu	Monazite	U–Pb	22.9	(15)
13	Wagye La	Monazite	U–Pb	11.9	(15)
14	Masang Kang-Paro	Monazite	U–Pb	13.0; 14.0; 23.0; 24.0	(2)
15	Khula Kangri	Monazite	U–Pb	12.5	(16)
17	Gonto La (Luozha)	Muscovite	K–Ar; Rb–Sr	12.4; 15.1; 15.8	(8, 17)
19	Quzhen	Whole rock	K–Ar	14.6	(18)
21	Hajinsangre (Kampa)	Biotite	Ar-Ar	13.74; 13.8	(19)
22	Kuday (Wing, Kua, Donggong)	Zircon	U–Pb	27.5; 28.1; 27.5; 14.5; 16.2	(20, 21, 22)
		Xenotime	U–Pb	22.6	(21)
		Biotite	Ar–Ar	10.5; 12.1; 11.5; 11.9; 12.5; 14.4; 13.5; 11.6; 14.1; 13.5; 13.6	(21, 23)
		Muscovite	Ar–Ar	13.5	(23)
23	Kouwu (Lijun, Gomdre)	Monazite	U–Pb	14.4; 14.5	(20)
		Zircon	U–Pb	14.4; 25.4; 14.2	(20, 21, 23)
		Xenotime	U–Pb	14.4	(21)
		Biotite	Ar–Ar	11.4; 8.8; 12.5	(20, 21, 23)
		Xenotime and Monazite	U–Pb	14.5	(23)
24	majia	Monazite	U–Pb	9.8; 9.2; 9.5	(10, 14)
		Xenotime	U–Pb	11.2	(21)
		Xenotime and Monazite	U–Pb	8.8	(21)
		Zircon	U–Pb	23.1	(23)
		Biotite	Ar–Ar	8.0; 8.6; 8.8	(21, 24)
		Muscovite	Ar–Ar	6.4	(24)
25	Lhagoi Kangri	Monazite and zircon	U–Pb	15.1; 14.7	(10, 25)
27	Xiaru	Muscovite	K–Ar	16.2	(8)
28	Malashan-Cuobu	Monazite	U–Pb	18.6; 17.8	(26)
		Zircon	U–Pb	19.3	(27)
29	Qiazuweng	Muscovite	K–Ar	17.4	(8)
30	Changguo	Muscovite	K–Ar	16.8	(8)
33	Dlou-Mugu	Monazite	U–Pb	17.6	(4)
	Zanskar	Monazite	U–Pb	20.0; 20.8; 19.5; 21.4	(28, 29)

Table 2
Modal abundances of the Himalayan leucogranites (%).

Body no.	Sample no.	Body name	Rock type	Pl	Kf	Bt	Mu	Tur	Qtz	Accessory minerals
5	J-G4	Gyirong	Tg	34	24		6.4	3.4	31	Ap + Zr + Gt + Mag
5	J-G7	Gyirong	Tg	25	27		7.1	4.6	37	Ap + Zr + Mon + Mag
5	J-G16	Gyirong	Tg	31	30	0.7	5.2	3.2	30	Ap + Zr + Mon
5	J-G2	Gyirong	Tg	26	25		3.8	5.9	38	Ap + Zr + Gt + Mag + Mon
7	NL-12	Nyalam	Tg	34	32		6.3	1.7	25	Ap + Zr + Mag
7	NL-25	Nyalam	Tg	30	37		8.3	2.4	22	Ap + Zr
7	NL-36	Nyalam	Tg	27	36		2.4	5.2	28	Ap + Zr + Mon
7	NL-03	Nyalam	Tg	26	40		5.7	3.6	23	Ap + Zr + Mag + Gt
7	NL-31	Nyalam	Tg	32	34		4.2	2.1	27	Ap + Zr + Mag
7	N-702	Nyalam	2 mg	35	31	5.6	6.9		20	Ap + Zr + Mag
7	NL-07	Nyalam	2 mg	32	25	4.3	8.5		29	Ap + Zr
10	DZ-15	Dinggye	2 mg	23	40	3.2	5.7		27	Ap + Zr + Mon + Mag
10	DG-2	Dinggye	2 mg	26	37	4.1	7.9		24	Ap + Zr + Mag
10	DG-08	Dinggye	Tg	26	40	0.8	2.4	3.7	25	Ap + Zr + Gt + Mon + Mag
10	DG-24	Dinggye	Tg	21	38		3.0	4.1	32	Ap + Zr + Mon
12	GP-05	Gaowu	2 mg	18	32	2.2	8.3	0.5	36	Ap + Zr + Mag
12	GP-09	Gaowu	2 mg	26	30	2.7	7.0		34	Ap + Mon + Mag
12	GU-8	Gaowu	2 mg	29	28	4.8	6.9		30	Ap + Mon + Mag
12	GG-2	Gaowu	2 mg	30	29	5.3	5.7		28	Ap + Zr + Mag
12	GF-6	Gaowu	Tg	24	36		4.6	2.7	31	Ap + Zr + Mag
12	GZ-7	Gaowu	Tg	33	29		2.0	3.5	32	Ap + Zr + Gt + Mag
17	LG-17	Luozha	2 mg	30	29	5.2	4.9		28	Zr + Ap + Tur + Mag
17	LG-02	Luozha	2 mg	34	27	7.3	5.6		24	Zr + Mon + Mag
17	LG-29	Luozha	2 mg	32	35	4.6	2.5		25	Zr + Ap + Mag + Mon
17	LG-06	Luozha	2 mg	21	38	4.8	2.7		32	Zr + Ap + Mon + Tur
19	ZF-31	Quzhen	2 mg	36	27	4.9	2.8		28	Ap + Zr + Mag
19	ZF-26	Quzhen	2 mg	29	35	4.7	3.3		27	Ap + Mon + Mag
19	ZF-18	Quzhen	2 mg	33	28	4.3	3.5		30	Ap + Zr + Mag
19	ZF-38	Quzhen	Tg	30	34	1.1	3.6	2.5	28	Ap + Zr + Gt + Mag

Body no. refers to number of the leucogranite in Fig. 1. Modal abundances were determined by point counting petrographic sections (for more details see the text). Ap: Apatite; Bt: Biotite; Gt: Garnet; Kf: K-feldspar; Mag: Magnetite; Mon: Monazite; Mu: Muscovite; Pl: Plagioclase; Qtz: Quartz; Tur: Tourmaline; Zr: Zircon. Tg: tourmaline granites; 2 mg: two-mica granites.

Notes to Table 1. Body no. refers to number of the leucogranite body in Fig.1.Data sources: (1) Harrison et al. (1997); (2) Searle and Godin (2003); (3) Hodges et al. (1996); (4) Harrison et al. (1999); (5) Harrison et al. (1995); (6) Deniel et al. (1987); (7) Guillot et al. (1994); (8) Liao et al. (2003); (9) Searle et al. (1997); (10) Scharer et al. (1986); (11) Murphy and Harrison (1999); (12) Scharer (1984); (13) Streule et al. (2010); (14) Liu et al. (1990); (15) Wu et al. (1998); (16) Edwards and Harrison (1997); (17) Tong et al. (2003); (18) Liao et al. (2006); (19) Quigley et al. (2006); (20) Zhang et al. (2004); (21) King et al. (2011); (22) Lee and Whitehouse (2007); (23) Lee et al. (2006); (24) Malaski et al. (1988); (25) Zhang et al. (2005); (26) Aoya et al. (2005); (27) Kawakami et al. (2007); (28) Noble and Searle (1995); (29) Dezes et al. (1999).

Table 3
Major and trace element contents of the Himalayan leucogranites.

Body no.	5	5	5	5	7	7	7	7
Sample no.	J-G4	J-G7	J-G16	J-G2	NL-12	NL-25	NL-36	NL-03
Body name	Gyirong	Gyirong	Gyirong	Gyirong	Nyalam	Nyalam	Nyalam	Nyalam
Rock type	Tg	Tg	Tg	Tg	Tg	Tg	Tg	Tg
Age (Ma)	16.11	16.11	16.11	16.11	16.8	16.8	16.8	16.8
SiO_2	72.20	74.06	74.59	75.32	74.16	73.08	75.24	73.76
TiO_2	0.08	0.05	0.05	0.04	0.11	0.08	0.06	0.05
Al_2O_3	14.19	15.12	15.06	14.29	15.40	15.23	14.83	15.07
TFe_2O_3	0.67	0.69	0.62	0.61	1.35	1.12	0.70	0.48
MnO	0.04	0.03	0.02	0.03	0.02	0.04	0.03	0.02
MgO	0.08	0.07	0.06	0.08	0.13	0.11	0.02	0.03
CaO	0.95	0.73	0.51	0.42	0.57	0.91	0.64	0.35
Na_2O	5.23	4.36	4.28	4.69	3.70	4.11	3.86	4.10
K_2O	4.95	4.35	4.66	4.22	4.06	4.46	3.95	4.53
P_2O_5	0.23	0.20	0.22	0.21	0.15	0.13	0.22	0.18
LOI	0.92	0.64	0.35	0.37	0.28	0.43	0.51	1.17
Total	99.54	100.30	100.42	100.28	99.93	99.70	100.06	99.74
La	2.46	6.05	3.72	5.14	5.36	2.58	6.51	3.86
Ce	4.38	9.39	7.04	9.51	10.73	5.87	12.32	7.34
Pr	0.62	1.02	0.87	1.13	1.31	0.68	1.44	0.93
Nd	2.73	3.91	3.97	4.34	5.56	3.11	5.83	3.66
Sm	0.66	1.15	1.13	1.18	1.58	0.96	1.75	1.03
Eu	0.14	0.26	0.21	0.24	0.35	0.18	0.29	0.22
Gd	0.77	1.43	1.48	1.52	1.54	0.87	1.42	1.13
Tb	0.18	0.27	0.31	0.28	0.26	0.17	0.24	0.22
Dy	1.24	1.66	1.97	1.78	1.45	0.98	1.29	1.18
Ho	0.26	0.33	0.35	0.37	0.25	0.18	0.22	0.20
Er	0.67	0.92	0.85	1.01	0.60	0.47	0.51	0.49
Tm	0.10	0.13	0.12	0.15	0.08	0.07	0.07	0.07
Yb	0.66	0.88	0.74	0.98	0.51	0.45	0.44	0.43
Lu	0.08	0.12	0.11	0.15	0.07	0.06	0.07	0.07
Sc	2.87	1.03	0.78	0.92	1.32	1.74	2.05	1.75
V	4.07	2.71	1.64	0.83	5.27	13.99	6.87	6.01
Cr	45.14	22.72	41.35	20.43	21.08	11.85	13.38	15.72
Co	0.89	0.54	0.70	0.42	1.16	1.49	1.22	4.39
Ni	14.01	2.31	6.92	2.19	21.90	13.02	17.30	10.29
Cu	8.71	10.02	16.08	6.11	5.64	10.71	6.91	8.30
Zn	44.38	57.42	29.14	38.70	35.21	23.40	19.32	20.06
Rb	568.42	321.71	452.20	510.17	381.32	479.52	472.65	656.61
Sr	37.81	41.35	68.33	34.71	27.09	77.11	98.79	112.18
Y	6.79	10.34	11.74	9.29	5.28	3.86	5.77	5.80
Zr	31.69	27.57	35.23	20.83	55.80	44.23	47.29	50.10
Nb	8.03	6.70	4.25	6.61	15.97	18.09	16.20	10.11
Ba	123.90	127.09	191.92	106.34	200.69	152.97	239.35	162.43
Hf	1.76	1.15	1.13	1.54	2.13	2.06	1.81	1.60
Ta	1.24	1.36	1.02	1.28	1.46	1.34	1.01	0.82
Pb	45.89	66.73	63.16	52.44	32.43	39.54	32.69	53.21
Th	2.34	2.16	2.62	2.10	3.15	3.58	4.82	4.19
U	6.87	9.51	12.19	6.89	8.32	10.50	9.07	15.18

Body no.	7	7	7	10	10	10	10
Sample no.	NL-31	N-702	NL-07	DZ-15	DG-2	DG-08	DG-24
Body name	Nyalam	Nyalam	Nyalam	Dinggye	Dinggye	Dinggye	Dinggye
Rock type	Tg	2 mg	2 mg	2 mg	2 mg	Tg	Tg
Age (Ma)	16.8	16.8	16.8	15.0	15.0	15.0	15.0
SiO_2	74.57	74.64	72.33	74.56	74.03	72.96	74.68
TiO_2	0.08	0.15	0.16	0.09	0.12	0.05	0.06
Al_2O_3	14.09	13.55	13.82	13.78	14.11	14.62	14.94
TFe_2O_3	0.96	1.42	1.54	1.23	1.27	1.13	0.95
MnO	0.03	0.02	0.05	0.04	0.02	0.03	0.01
MgO	0.09	0.28	0.37	0.22	0.25	0.18	0.11
CaO	0.68	1.02	1.18	0.76	0.81	0.58	0.52
Na_2O	4.55	3.65	3.59	3.38	3.47	4.89	4.48
K_2O	4.21	4.63	5.21	4.97	5.08	4.67	3.89
P_2O_5	0.16	0.06	0.10	0.11	0.08	0.23	0.17
LOI	0.46	0.97	1.23	0.66	0.42	0.49	0.32
Total	99.88	100.39	99.58	99.80	99.66	99.83	100.13
La	5.39	16.88	11.72	4.69	5.01	2.74	3.49
Ce	10.58	32.72	25.81	8.78	10.43	6.06	6.58
Pr	1.27	3.29	2.77	1.31	1.22	0.89	0.71
Nd	5.21	14.26	11.08	6.12	5.44	4.46	3.25
Sm	1.46	3.54	3.23	1.97	1.72	1.35	0.74

(continued on next page)

Table 3 (*continued*)

Body no.	7	7	7	10	10	10	10
Sample no.	NL-31	N-702	NL-07	DZ-15	DG-2	DG-08	DG-24
Body name	Nyalam	Nyalam	Nyalam	Dinggye	Dinggye	Dinggye	Dinggye
Rock type	Tg	2 mg	2 mg	2 mg	2 mg	Tg	Tg
Age (Ma)	16.8	16.8	16.8	15.0	15.0	15.0	15.0
Eu	0.31	0.51	0.49	0.26	0.22	0.12	0.13
Gd	1.43	3.04	2.48	1.83	1.29	1.47	1.07
Tb	0.26	0.52	0.39	0.42	0.31	0.35	0.23
Dy	1.45	2.98	1.87	2.73	2.05	2.22	1.45
Ho	0.24	0.52	0.33	0.56	0.41	0.46	0.28
Er	0.61	1.21	0.82	1.52	1.03	1.29	0.81
Tm	0.09	0.16	0.11	0.24	0.15	0.20	0.12
Yb	0.53	1.02	0.64	1.57	0.92	1.32	0.79
Lu	0.08	0.13	0.10	0.21	0.14	0.20	0.11
Sc	1.66	2.33	2.57	2.38	2.70	1.18	1.20
V	9.15	10.31	11.35	9.74	11.57	2.35	2.04
Cr	13.60	20.02	26.79	21.72	15.90	8.30	26.29
Co	5.88	3.47	1.82	2.70	2.29	0.51	0.68
Ni	10.83	15.70	22.90	3.37	5.02	1.98	13.11
Cu	6.24	8.29	11.23	6.79	4.21	2.37	3.05
Zn	21.94	23.97	41.60	17.96	22.01	20.19	16.30
Rb	320.16	268.17	218.69	95.86	102.37	325.90	416.36
Sr	39.74	108.41	89.02	57.28	44.43	59.58	53.74
Y	6.12	17.39	15.84	15.60	16.39	8.32	9.77
Zr	43.18	79.26	110.21	65.12	44.73	42.80	26.14
Nb	8.28	14.37	13.92	12.05	14.01	9.47	8.52
Ba	56.39	488.02	539.42	212.40	351.90	154.21	108.35
Hf	1.14	2.59	3.27	3.17	2.58	1.29	0.86
Ta	1.19	2.67	1.92	2.16	1.82	0.73	1.45
Pb	37.33	34.38	41.09	52.88	45.30	25.87	20.81
Th	3.07	21.53	16.26	8.37	9.42	2.39	2.70
U	4.24	7.06	9.08	7.81	8.83	8.81	10.17
Body no.	12	12	12	12	12	12	17
Sample no.	GP-05	GP-09	GU-8	GG-2	GF-6	GZ-7	LG-17
Body name	Gaowu	Gaowu	Gaowu	Gaowu	Gaowu	Gaowu	Luozha
Rock type	2 mg	2 mg	2 mg	2 mg	Tg	Tg	2 mg
Age (Ma)	22.9	22.9	22.9	22.9	22.9	22.9	14.4
SiO_2	73.39	72.05	70.56	70.87	73.09	74.01	73.47
TiO_2	0.08	0.13	0.21	0.16	0.04	0.03	0.19
Al_2O_3	14.12	15.23	14.78	15.39	15.67	14.72	13.93
TFe_2O_3	1.87	2.13	2.64	2.16	1.03	0.92	1.52
MnO	0.04	0.02	0.04	0.03	0.02	0.03	0.03
MgO	0.26	0.31	0.43	0.38	0.15	0.17	0.29
CaO	1.32	1.06	1.42	1.74	0.55	0.49	1.48
Na_2O	3.55	3.51	3.69	3.56	4.48	4.61	3.69
K_2O	4.51	4.87	4.91	4.69	4.49	4.66	4.60
P_2O_5	0.15	0.18	0.21	0.10	0.17	0.15	0.07
LOI	0.67	0.98	0.85	0.68	0.49	0.32	0.58
Total	99.96	100.47	99.74	99.76	100.18	100.11	99.85
La	9.13	10.16	11.59	18.66	6.34	3.83	15.29
Ce	15.91	20.06	17.83	39.39	10.66	7.02	24.42
Pr	1.74	2.26	2.06	4.11	1.16	0.85	2.94
Nd	6.91	8.43	7.69	15.07	4.03	3.89	12.78
Sm	2.27	2.54	2.62	4.14	1.01	1.13	3.81
Eu	0.28	0.38	0.42	0.67	0.13	0.08	0.52
Gd	1.54	2.03	2.28	3.43	1.15	1.23	2.47
Tb	0.26	0.32	0.34	0.46	0.22	0.19	0.38
Dy	1.35	1.48	1.61	2.53	1.18	1.06	2.32
Ho	0.24	0.24	0.27	0.43	0.20	0.21	0.43
Er	0.57	0.58	0.59	1.15	0.51	0.54	0.98
Tm	0.08	0.08	0.08	0.16	0.07	0.08	0.12
Yb	0.48	0.51	0.52	1.02	0.40	0.47	0.79
Lu	0.07	0.07	0.08	0.13	0.06	0.07	0.12
Sc	1.78	3.09	3.09	2.68	1.70	1.02	3.17
V	6.07	7.93	10.75	11.20	3.96	2.13	25.29
Cr	10.28	15.17	28.51	26.09	10.32	8.45	16.82
Co	1.21	2.90	4.06	2.65	0.78	0.91	3.48
Ni	12.80	16.75	21.57	17.45	1.77	2.18	5.63
Cu	5.24	8.36	10.32	8.43	3.11	2.09	7.30
Zn	20.81	32.42	45.11	39.80	26.30	34.12	46.09
Rb	281.27	349.14	212.71	294.55	446.90	269.52	223.14

Table 3 (*continued*)

Body no.	12	12	12	12	12	12	17
Sample no.	GP-05	GP-09	GU-8	GG-2	GF-6	GZ-7	LG-17
Body name	Gaowu	Gaowu	Gaowu	Gaowu	Gaowu	Gaowu	Luozha
Rock type	2 mg	2 mg	2 mg	2 mg	Tg	Tg	2 mg
Age (Ma)	22.9	22.9	22.9	22.9	22.9	22.9	14.4
Sr	76.80	89.37	138.09	126.74	118.05	23.71	106.70
Y	8.26	13.07	23.05	20.57	5.42	3.19	15.80
Zr	68.05	74.31	95.97	86.14	35.78	22.10	95.75
Nb	28.17	21.85	29.70	30.65	18.85	14.57	10.71
Ba	286.81	258.13	515.03	437.69	241.50	77.18	238.19
Hf	1.94	3.56	3.37	4.19	1.26	1.08	2.69
Ta	4.42	5.85	2.07	3.88	2.54	3.37	1.74
Pb	23.87	56.18	30.15	48.29	65.11	26.25	25.86
Th	7.68	7.79	16.88	15.12	3.92	1.35	12.68
U	11.52	7.43	5.37	4.69	16.37	4.86	3.70
Body no.	17	17	17	19	19	19	19
Sample no.	LG-02	LG-29	LG-06	ZF-31	ZF-26	ZF-18	ZF-38
Body name	Luozha	Luozha	Luozha	Quzhen	Quzhen	Quzhen	Quzhen
Rock type	2 mg	2 mg	2 mg	2 mg	2 mg	2 mg	Tg
Age (Ma)	14.4	14.4	14.4	14.65	14.65	14.65	14.65
SiO_2	71.68	72.39	74.58	72.53	73.28	73.96	74.65
TiO_2	0.22	0.18	0.13	0.12	0.14	0.13	0.11
Al_2O_3	14.31	14.86	14.56	14.39	15.01	14.26	15.37
TFe_2O_3	1.89	1.65	1.57	1.35	1.16	1.02	0.78
MnO	0.02	0.04	0.02	0.04	0.03	0.02	0.03
MgO	0.46	0.35	0.17	0.25	0.15	0.14	0.20
CaO	1.63	1.26	1.13	0.76	0.87	0.96	0.63
Na_2O	4.24	3.43	3.36	4.57	4.18	3.91	4.36
K_2O	4.48	4.65	4.39	5.18	4.36	4.19	3.74
P_2O_5	0.11	0.09	0.06	0.07	0.10	0.08	0.12
LOI	0.75	0.94	0.47	0.59	0.62	0.87	0.45
Total	99.79	99.84	100.44	99.85	99.90	99.54	100.44
La	34.37	32.86	19.42	26.18	27.02	22.79	24.48
Ce	72.15	49.01	32.37	53.16	52.25	42.15	47.89
Pr	7.69	5.47	3.76	6.06	5.43	4.57	6.16
Nd	28.48	23.16	12.45	22.57	18.23	15.76	20.35
Sm	6.15	5.93	3.05	4.63	3.59	3.11	4.15
Eu	0.86	0.56	0.50	0.76	0.37	0.48	0.55
Gd	4.83	4.41	3.12	3.27	3.08	2.75	3.26
Tb	0.63	0.72	0.43	0.42	0.41	0.36	0.42
Dy	2.66	3.28	1.94	2.03	1.89	1.73	1.78
Ho	0.32	0.49	0.35	0.35	0.28	0.29	0.27
Er	0.71	1.15	0.92	0.79	0.62	0.55	0.55
Tm	0.10	0.16	0.14	0.10	0.08	0.06	0.07
Yb	0.67	0.98	0.90	0.62	0.43	0.36	0.41
Lu	0.10	0.14	0.13	0.09	0.06	0.05	0.05
Sc	3.64	2.71	4.85	3.17	2.36	1.95	2.28
V	38.01	16.19	21.67	13.08	10.52	18.41	7.35
Cr	27.38	38.23	13.69	15.38	8.43	10.11	6.39
Co	5.19	4.89	2.54	6.38	3.77	5.16	4.29
Ni	9.80	11.53	4.85	8.34	15.30	7.79	6.29
Cu	13.07	5.46	3.70	17.28	8.39	12.51	9.40
Zn	45.27	59.49	41.18	54.91	40.18	48.62	37.29
Rb	169.37	186.42	204.69	289.44	327.58	335.80	362.11
Sr	145.67	134.58	74.72	116.52	67.85	116.72	109.46
Y	12.79	21.41	8.42	11.86	8.35	12.51	5.48
Zr	71.53	84.05	62.43	63.90	76.21	67.15	66.29
Nb	15.35	12.53	9.20	15.47	9.48	13.38	10.82
Ba	517.49	302.76	145.61	403.16	421.74	385.23	426.53
Hf	3.57	2.64	2.80	1.25	2.31	1.39	1.62
Ta	1.96	2.87	1.58	2.67	2.18	3.35	1.77
Pb	54.08	40.62	21.15	56.30	25.72	41.33	27.54
Th	15.97	10.38	11.82	11.19	15.47	14.35	5.73
U	4.58	9.16	2.83	9.03	4.18	7.32	8.66

LOI = loss on ignition. Total represents sum of major element oxide contents (including LOI). Age (Ma) is the weighted average age of the leucogranites calculated from all of the age data in the published literature (Table 1). Body no. refers to number of the leucogranite body in Fig. 1. TFe_2O_3 = total Fe is given as Fe_2O_3. Tg: tourmaline granites; 2 mg: two-mica granites.

Table 4
Sr–Nd isotope compositions of the Himalayan leucogranites.

Body no.	Sample no.	Body name	$^{87}Sr/^{86}Sr \pm 2\sigma$	$^{143}Nd/^{144}Nd \pm 2\sigma$	$(^{87}Sr/^{86}Sr)_i$	$(^{143}Nd/^{144}Nd)_i$
5	J-G4	Gyirong	0.805152 ± 11	0.511775 ± 6	0.795106	0.511757
5	J-G7	Gyirong	0.764437 ± 13	0.511813 ± 10	0.759258	0.511795
5	J-G16	Gyirong	0.789032 ± 13	0.511728 ± 5	0.784616	0.511711
5	J-G2	Gyirong	0.796708 ± 9	0.511712 ± 8	0.786894	0.511693
7	NL-12	Nyalam	0.761095 ± 16	0.511717 ± 8	0.751328	0.511700
7	NL-25	Nyalam	0.776032 ± 13	0.511718 ± 6	0.771711	0.511700
7	NL-36	Nyalam	0.755964 ± 12	0.511776 ± 11	0.752646	0.511758
7	NL-03	Nyalam	0.772143 ± 17	0.511749 ± 9	0.768077	0.511730
7	NL-31	Nyalam	0.767136 ± 19	0.511854 ± 7	0.761542	0.511835
7	N-702	Nyalam	0.748326 ± 14	0.511842 ± 9	0.746612	0.511823
7	NL-07	Nyalam	0.741938 ± 11	0.511819 ± 12	0.740236	0.511801
10	DZ-15	Dinggye	0.776943 ± 7	0.511801 ± 10	0.775905	0.511787
10	DG-2	Dinggye	0.797401 ± 12	0.511838 ± 13	0.795968	0.511824
10	DG-08	Dinggye	0.783094 ± 8	0.511772 ± 10	0.779698	0.511755
10	DG-24	Dinggye	0.802116 ± 10	0.511805 ± 8	0.797297	0.511788
12	GP-05	Gaowu	0.770283 ± 9	0.511889 ± 9	0.766816	0.511867
12	GP-09	Gaowu	0.788309 ± 13	0.511857 ± 12	0.784604	0.511836
12	GU-8	Gaowu	0.733469 ± 12	0.511792 ± 7	0.732016	0.511770
12	GG-2	Gaowu	0.757376 ± 16	0.511809 ± 6	0.755178	0.511787
12	GF-6	Gaowu	0.768546 ± 14	0.511872 ± 8	0.764963	0.511850
12	GZ-7	Gaowu	0.794827 ± 10	0.511828 ± 9	0.784039	0.511806
17	LG-17	Luozha	0.744316 ± 13	0.511791 ± 7	0.743074	0.511777
17	LG-02	Luozha	0.749258 ± 17	0.511806 ± 7	0.748567	0.511792
17	LG-29	Luozha	0.746031 ± 16	0.511774 ± 8	0.745208	0.511761
17	LG-06	Luozha	0.725625 ± 12	0.511849 ± 9	0.724001	0.511835
19	ZF-31	Quzhen	0.768905 ± 11	0.511904 ± 9	0.767401	0.511893
19	ZF-26	Quzhen	0.729351 ± 9	0.511917 ± 7	0.726439	0.511906
19	ZF-18	Quzhen	0.736713 ± 10	0.511878 ± 6	0.734976	0.511867
19	ZF-38	Quzhen	0.741164 ± 15	0.511762 ± 8	0.739166	0.511747

Body no. refers to the number of the leucogranite body in Fig. 1.
Chondritic uniform reservoir (CHUR) at the present day [$(^{87}Rb/^{86}Sr)_{CHUR} = 0.0847$ (McCulloch and Black, 1984); $(^{87}Sr/^{86}Sr)_{CHUR} = 0.7045$ (DePaolo, 1988); $(^{147}Sm/^{144}Nd)_{CHUR} = 0.1967$ (Jacobsen and Wasserburg, 1980); $(^{143}Nd/^{144}Nd)_{CHUR} = 0.512638$ (Goldstein et al., 1984)] was used for the calculations. $\lambda_{Rb} = 1.42 \times 10^{-11}$ year^{-1} (Steiger and Jager, 1977); $\lambda_{Sm} = 6.54 \times 10^{-12}$ year^{-1} (Lugmair and Marti, 1978).
Initial Sr and Nd isotope ratios were obtained by using the average age as in Table 3.

4. Analytical methods

To obtain homogeneous whole-rock powders, ~3 kg of each of the leucogranite samples were selected. On a basis of petrographic observations, twenty-nine samples were cut into thin slices and powdered in an agate mortar for whole-rock major element, trace element and Sr–Nd isotope analysis.

4.1. Whole rock major and trace element analyses

Major element contents were analyzed using a Phillips PW1400 sequential X-ray fluorescence spectrometer (XRF) at the Institute of Geology and Geophysics, Chinese Academy of Sciences, Beijing, China (IGGCAS). Sample powders (1.2 g) were fused with $Li_2B_4O_7$ (6 g) in a fusion furnace at 1050 °C for 20 min. Loss on ignition (LOI) was determined by ignition at 1000 °C for 10 h for 2 g powders. Analytical precision was better than 2% relative. Detailed analytical procedures follow those reported by Guo et al. (2006, 2007). Analytical data are presented in Table 3.

Rare earth element (REE) and trace element analyses were made by inductively coupled plasma mass spectrometer (ICP-MS) using a Finnigan MAT Element I system at IGGCAS. Sample powders (40 mg) were dissolved in distilled 1 ml HF and 0.5 ml HNO_3 in 7 ml Savillex Teflon screw-cap capsules. The solutions were evaporated at 150 °C to dryness and the residue digested with 1.5 ml HF and 0.5 ml HNO_3, and heated at 170 °C for 10 days, dried and redissolved in 2 ml HNO_3 in the capsules. Then, the solutions were put into plastic beakers and 1 ml 500 ppb In was added as an internal standard. Finally, the solutions were diluted in 1% HNO_3 to 50 ml for analysis. Total procedural blank solutions were <50 ng for the trace elements in Table 3. During the analytical runs, frequent standard calibrations were performed to correct for instrumental signal drift. Precision, based on repeated analyses of samples and international standards (BHVO-1 and AGV-1), is less than 5% for all the elements reported in Table 3. Detailed analytical procedures follow those of Guo et al. (2005, 2006).

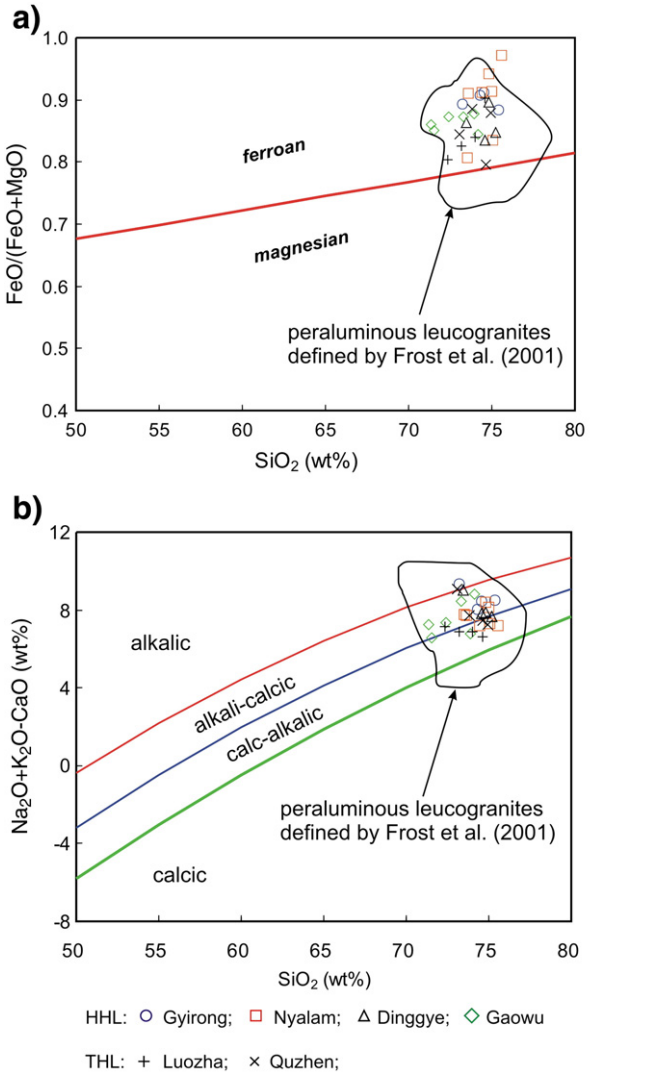

Fig. 2. (a) Classification diagram of FeO/(FeO + MgO) vs SiO_2 (wt.%) for the Himalayan leucogranites (Frost et al., 2001). The ferroan-magnesian division (red line) is from Frost et al. (2001). All data plotted have been recalculated to 100 wt.% on a volatile-free basis. (b) $Na_2O + K_2O$-CaO (wt.%) vs SiO_2 (wt.%) diagram for the same samples plotted in (a). Data have been normalized to 100 wt.% volatile-free as indicated in Table 3. The dividing lines show the classification boundaries from Frost et al. (2001). Data sources and symbols are as in (a).

4.2. Sr and Nd isotope analyses

Sr–Nd isotope analysis was performed on a Finnigan MAT262 mass spectrometer at IGGCAS. Sample powders (60 mg) were spiked with mixed isotope tracers (^{87}Rb–^{84}Sr and ^{149}Sm–^{150}Nd), then dissolved with a mixed acid ($HF:HClO_4 = 3:1$) in Teflon capsules for 7 days at room temperature. Rb, Sr, Sm and Nd were separated from other rare earth element fractions in solution using AG50W × 8 (H^+) cationic ion-exchange resin columns. Collected Sr and Nd fractions were evaporated and dissolved in 2% HNO_3 for analysis by mass spectrometry. Mass fractionation corrections were based on $^{86}Sr/^{88}$

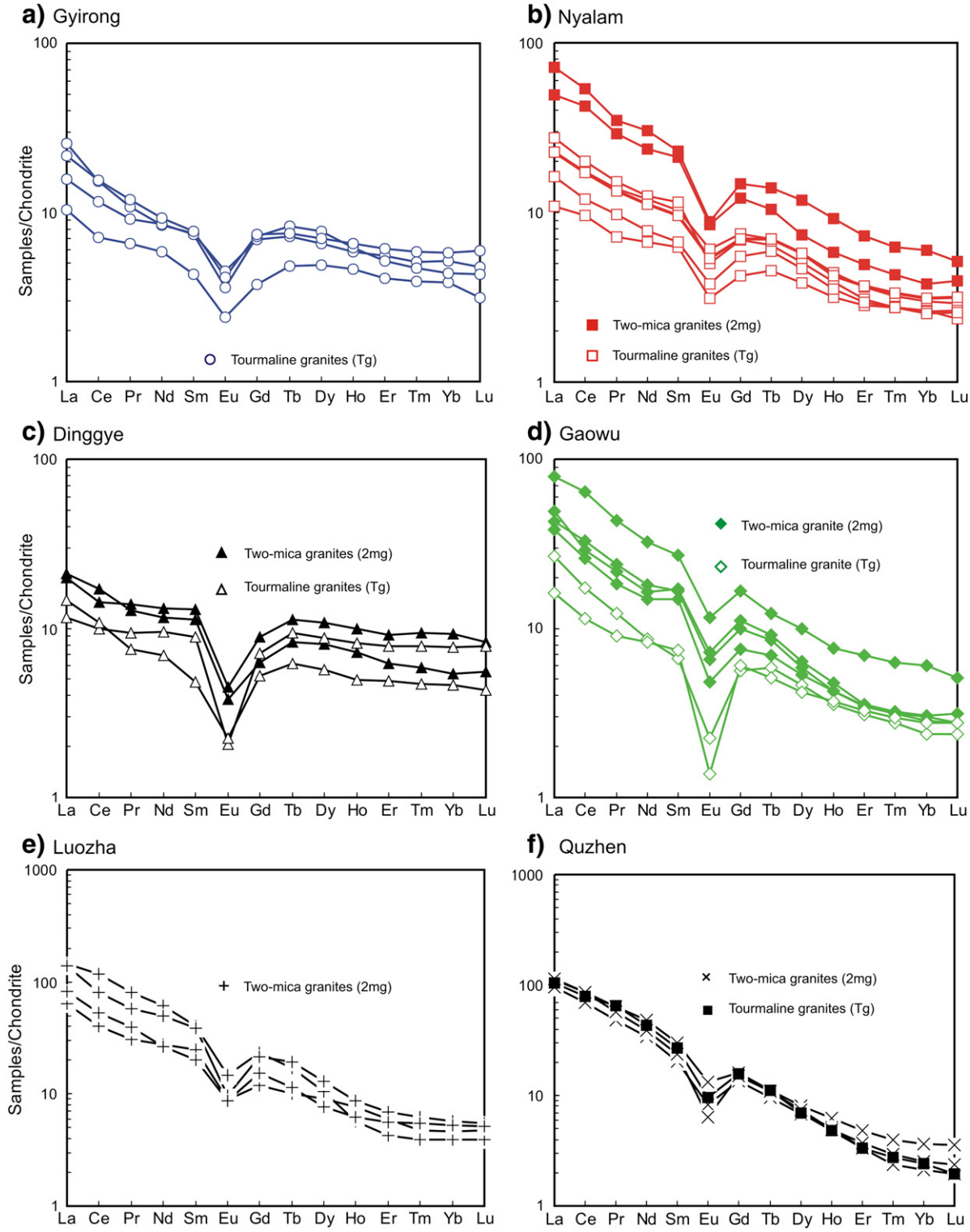

Fig. 3. Chondrite-normalized rare earth element diagrams; normalization factors are from Sun and McDonough (1989). (a) Gyirong; (b) Nyalam; (c) Dinggye; (d) Gaowu; (e) Luozha; (f) Quzhen.

Sr = 0.1194 and $^{146}Nd/^{144}Nd = 0.7219$. International standard NBS987 gave $^{87}Sr/^{86}Sr = 0.710254 \pm 16$ (n = 8) and NBS607 yielded $^{87}Sr/^{86}Sr = 1.20032 \pm 30$ (n = 12); La Jolla gave $^{143}Nd/^{144}Nd = 0.511862 \pm 7$ (n = 12) and BCR-1 yielded $^{143}Nd/^{144}Nd = 0.512626 \pm 9$ (n = 12). The whole procedure blank is less than 2×10^{-10} g for Rb–Sr and 5×10^{-11} g for Sm–Nd isotope analysis. Analytical results and errors (2σ) are reported in Table 4. Initial $^{87}Sr/^{86}Sr$ and $^{143}Nd/^{144}Nd$ ratios (Table 4) were calculated using the average ages of the leucogranite bodies (Table 1) based on U–Pb, $^{40}Ar/^{39}Ar$, Rb–Sr and K–Ar dating. Detailed procedures for Sr–Nd isotope analysis follow those of Guo et al. (2006, 2007).

5. Results

Major element contents (Table 3) indicate that most of the leucogranites analyzed are peraluminous (ASI>1) to strongly peraluminous (ASI≥1.1) with an ASI (molecular ratio of $Al_2O_3/(CaO+Na_2O+K_2O)$) of 1.01–1.34, except for three metaluminous samples (J-G4, LG-02 and ZF-31) with an ASI<1 (0.90–0.99), based on the criteria of Sylvester (1998) and Barbarin (1999). The leucogranites studied have high SiO_2 (70.56–75.32 wt.%), Al_2O_3 (13.55–15.67 wt.%), and low MgO (0.02–0.46 wt.%) contents. The Na_2O (3.36–5.23 wt.%) concentrations are similar to those of K_2O (3.74–5.21 wt.%). Based on the classification of Frost et al. (2001), the rocks are ferroan (Fig. 2a) and alkalic to calc-alkalic (Fig. 2b), and plot within the field for peraluminous leucogranites. This indicates that they are crustal melts. Compared with the 2 mg, the Tg have higher Al_2O_3, Na_2O, P_2O_5 and Rb contents, and lower Fe_2O_3, MgO, CaO, K_2O, TiO_2, Ba, Sr, Th, Zr and Y contents at a given SiO_2 content (Table 3). The leucogranites are characterized by light REE (LREE) enrichment and moderate-strong negative Eu anomalies in chondrite-normalized rare earth element patterns (Fig. 3). The 2 mg are characterized by higher chondrite--normalized REE abundances compared to the Tg (Fig. 3), though with broadly similar patterns. Relative to the 2 mg, most Tg have lower ∑REE, LREE and HREE contents (Table 3), and lower La/Yb and Gd/Yb ratios (Fig. 3 and Table 3). The THL have higher REE concentrations than the HHL (Fig. 3). Leucogranites from Gyirong and Dinggye (Figs. 3a.c) have much flatter middle-heavy REE patterns than those from the other localities.

All the leucogranites show pronounced negative Ba, Sr, Nb and Ti anomalies and positive Rb, U, K, P and Pb anomalies in their primitive mantle-normalized trace element patterns (Fig. 4). The leucogranites have extremely high $(^{87}Sr/^{86}Sr)_i$ (0.724001–0.797297) and low $(^{143}Nd/^{144}Nd)_i$ (0.511693–0.511906) (Table 4 and Fig. 5). The Sr–Nd isotope data define a broad linear trend between the data fields for the HH and LH crustal sequences (Fig. 5).

6. Discussion

Detailed studies of the Himalayan leucogranites have provided important constraints on the tectonic evolution of the orogen (e.g. Visona and Lombardo, 2002; Searle and Godin, 2003; King et al., 2011). The geochemical characteristics of the leucogranites can also shed light on the nature of their crustal source region and the geodynamic setting of the magmatism.

6.1. Age of the Himalayan leucogranites

To elucidate the geodynamic setting of the Himalayan leucogranites we have compiled all the available geochronological data in the published literature (Table 1). A number of different dating methods (e.g. zircon U–Pb; $^{40}Ar/^{39}Ar$; Rb-Sr; K–Ar) have been employed (Table 1). We have checked the data quality and compared the ages from the different methods to constrain the age ranges of the leucogranites. These vary from 9 to 25 Ma (Table 1). The ages of the HHL (12–25 Ma) overlap those of the THL (9–18 Ma).

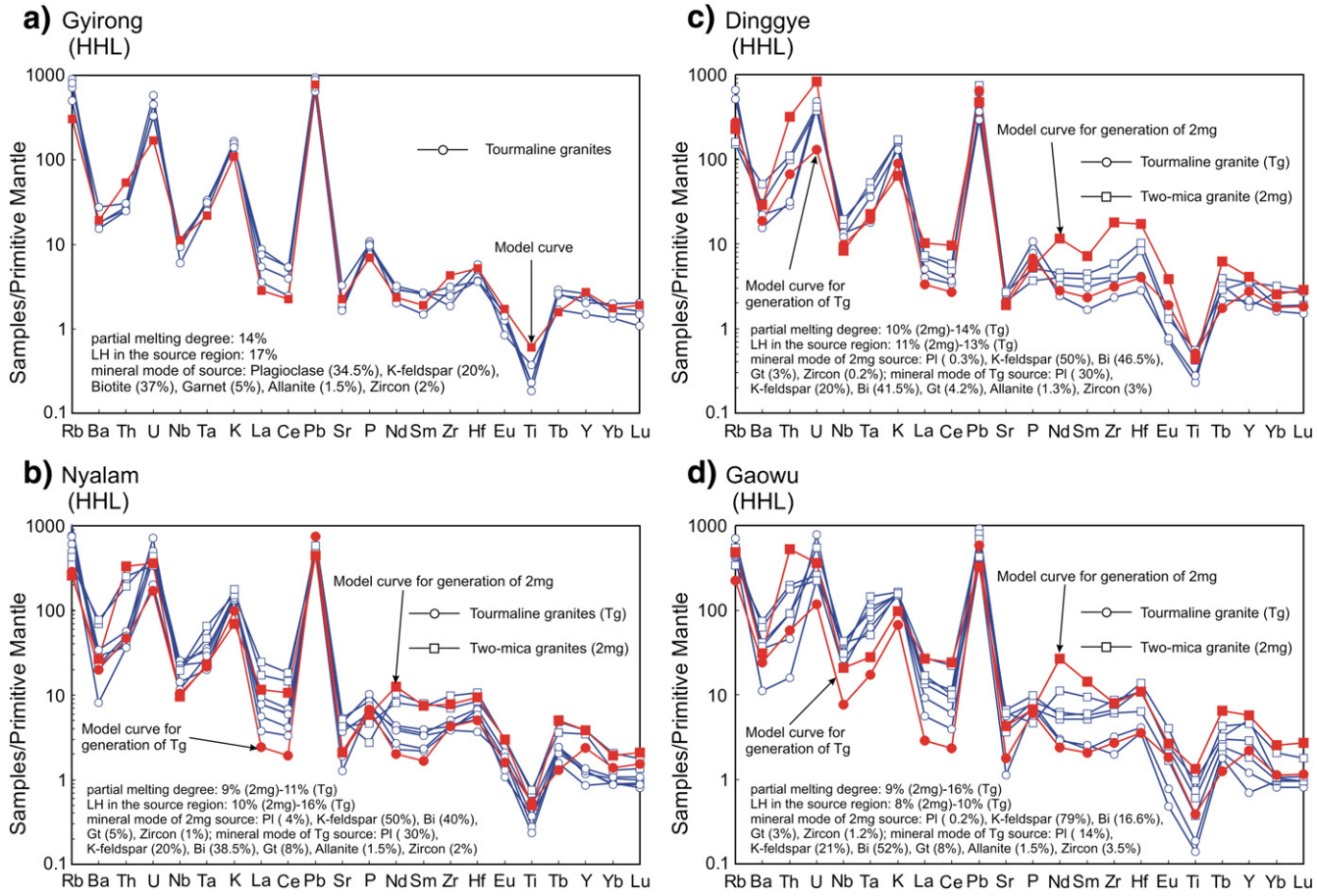

Fig. 4. Primitive mantle-normalized trace element diagrams; normalization factors are from Sun and McDonough (1989). They show the comparison between the observed data for the leucogranites and our model curves (red lines). The red curves with filled red squares and circles represent the results simulated by a non-modal batch melting model for the generation of 2 mg (two-mica granites) and Tg (tourmaline granites), respectively. (a) Gyirong; (b) Nyalam; (c) Dinggye; (d) Gaowu; (e) Luozha; (f) Quzhen. The detailed calculation procedures are explained in the text, Table 7 and Table 8.

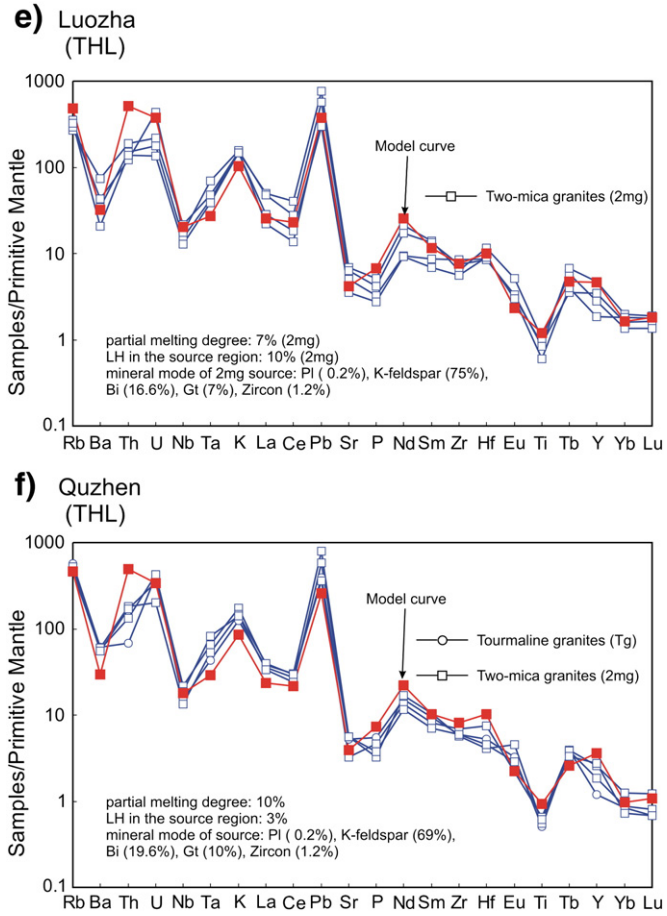

Fig. 4 (*continued*).

6.2. Source region of the Himalayan leucogranites

The Ce/Pb and Nb/U ratios of the leucogranites (Fig. 6) show little variation and are similar to those of the Upper Continental Crust (UCC; Taylor and McLennan, 1985) and the Bulk Continental Crust (BCC; Rudnick and Fountain, 1995). They have different Ce/Pb and Nb/U ratios from typical mantle values (Ce/Pb = 25 ± 5; Nb/U = 47 ± 10; Hofmann et al., 1986). This, together with their high SiO_2, Al_2O_3, $(^{87}Sr/^{86}Sr)_i$, and low MgO and $(^{143}Nd/^{144}Nd)_i$, suggest that they are crustal melts.

Previous studies (e.g. Ahmad et al., 2000; Richards et al., 2006) have indicated that the HH and LH crustal sequences were derived from isotopically distinct sources and that each preserves a distinct Sr–Nd isotope signature. Thus, comparison of the Sr–Nd isotope compositions of the HH sequence, LH sequence and Himalayan leucogranites should be an effective tool for identifying the source region of the leucogranites. The curvilinear trend of the leucogranites in a Sr–Nd isotope diagram (Fig. 5) indicates that the source region could have been a two-component mixture between the HH and LH sequences. Most of the leucogranites studied have overlapping Sr-Nd isotope ratios with the HH sequence (Fig. 5), suggesting that the contribution from the HH sequence was higher than that from the LH sequence.

Previous studies have shown that the combination of trace element and isotope ratios can be used effectively to fingerprint the type (fluid or melt) of components in a two-component mixed source of magmas (e.g. Hawkesworth et al., 1997; Turner et al., 1997). An aqueous fluid, which carries very little REE and Th, Nb, Zr and Ta, can introduce significant amounts of Rb, Ba, Sr, U, Pb into a mixed source region. In contrast, silicate melts are characterized by relatively high Th and LREE contents (Hawkesworth et al., 1997; Turner et al., 1997). Thus, those magmatic rocks whose source regions were strongly metasomatised by a fluid component are likely to have higher U/Th (Hawkesworth et al., 1997), Ba/Th (Hawkesworth et al., 1997; Turner et al., 1997) and Sr/Th (Hawkesworth et al., 1997) ratios than rocks whose source was enriched by a melt (Hawkesworth et al., 1997; Elburg et al., 2002). Both fluid- and melt-metasomatised two-component mixed source regions could have the same Sr–Nd isotope composition as the resultant magmas derived from these sources.

The leucogranites studied display negative linear correlations between Ba/Th and $(^{143}Nd/^{144}Nd)_i$, and Sr/Th and $(^{143}Nd/^{144}Nd)_i$ (Fig. 7), which is consistent with two-component mixing in the source region of the magmas. One end-member has a Sr–Nd isotope composition similar to that of the LH (Lesser Himalaya) sequence (e.g. Ahmad et al., 2000; Richards et al., 2006), but with higher Ba/Th and Sr/Th ratios than those of the LH sequence (Table 5 and Fig. 7). This indicates that a fluid derived from the LH sequence could be an end-member for the two-component mixed source region. The other end-member for the two-component mixing has a similar Sr–Nd isotope composition and Ba/Th and Sr/Th ratios to the HH (High Himalayan Crystalline) sequence (e.g. Inger and Harris et al., 1993; Ahmad et al., 2000; Richards et al., 2006) (Table 5 and Fig. 7). This end-member is likely an easily fusible lithology within the HH sequence. On the basis of the combined trace and Sr–Nd isotope data, we conclude that it is likely that the source region of the leucogranites is a two-component mixture between a fluid derived from the LH sequence and the bulk HH sequence.

To estimate quantitatively the relative proportions of the bulk HH sequence and a fluid derived from the LH sequence in the source region of the leucogranites, we have carried out Sr–Nd isotope two-component mixing calculations (Fig. 5). Based on previous studies (Ahmad et al., 2000; Richards et al., 2005), we consider that the fluid is derived from pelitic slates within the LH sequence, whilst biotite gneisses within the HH sequence represent the composition of the other end-member. The Sr–Nd isotope ratios and Nd and Sr concentrations in the bulk biotite gneiss were estimated as follows (after Richards et al., 2005): Sr = 122.0 ppm, $(^{87}Sr/^{86}Sr)_i = 0.742835$, Nd = 29.7 ppm and $(^{143}Nd/^{144}Nd)_i = 0.511969$. The Sr–Nd isotope composition in the fluid derived from the pelitic slate was assumed to be: $(^{87}Sr/^{86}Sr)_i = 0.947035$ and $(^{143}Nd/^{144}Nd)_i = 0.511266$ (Richards et al., 2005). The $(^{87}Sr/^{86}Sr)_i$ and $(^{143}Nd/^{144}Nd)_i$ data were both age-corrected to 10 Ma (in order to compare to the initial Sr–Nd isotope ratios of the Himalayan leucogranites).

Experimental studies (Kogiso et al., 1997; Aizawa et al., 1999; Johnson and Plank, 1999) and numerical simulations (e.g. Tatsumi and Hanyu, 2003) suggest that the first-order controlling factors on the concentrations of trace elements in an aqueous fluid derived from a metapelite source are the degree of element mobilization during dehydration processes, mineral-fluid partitioning of the trace elements and the bulk sediment composition. We estimate the Sr and Nd concentrations in the fluid based on previous observations of the degree of trace element mobilization during dehydration (e.g. Kogiso et al., 1997; Aizawa et al., 1999), the mineral-fluid partitioning of the trace elements of interest (e.g. Johnson and Plank, 1999) and the original composition of the bulk pelitic slate (Richards et al., 2005), using the calculation method of Tatsumi and Hanyu (2003). For further details of the calculations see Table 6. Our calculations suggest that the Sr and Nd concentrations in the fluid are 152.0 ppm and 83.4 ppm, respectively. The Sr concentration in the fluid is about 4 times higher than that in the bulk pelitic slate and the Nd content about 2 times higher. The Sr–Nd isotope two-component mixing model between the fluid derived from the pelitic slate (LH) and bulk biotite gneiss (HH) follows that of Faure and Mensing (2005).

The Sr–Nd isotope two-component mixing calculation indicates that the proportion of the fluid derived from the pelitic slate in the source region of the tourmaline leucogranites (Tg) and two-mica leucogranites (2 mg) is 6–19% and 2–12%, respectively (Fig. 5 and Table 6). The amount of the fluid derived from the pelitic slate within the LH sequence

in the source region of the HHL (including Tg and 2 mg) is 5–19% whereas for the THL (almost all 2 mg) this is 2–13% (Fig. 5). The amount of the fluid derived from the pelitic slate in the source region increases from north (THL) to south (HHL) (Fig. 1).

6.3. Trace element modeling

To quantitatively simulate leucogranite magma generation, we have carried out trace element modeling calculations using a non-modal batch melting model (Wilson, 1989; Guo et al., 2005, 2006). As noted earlier, the trace element characteristics of the leucogranites provide some useful constraints on the mineralogy of their source region. The negative Ba, Sr, Nb and Ti anomalies in their primitive mantle-normalized trace element patterns (Fig. 4) are consistent with the presence of residual plagioclase, K-feldspar and biotite in the source region. The relatively low LREE and HREE contents in the Tg (Fig. 4) suggest that allanite is also likely a residual mineral in the source region. The positive linear correlation between La/Yb and Gd/Yb (Fig. 8), together with the La/Yb increase with Gd/Yb from the HHL in the south to the THL in the north (Fig. 1 and Fig. 8), indicates that the amount of residual garnet in the source region of the leucogranites is higher in the THL than in the HHL. The relatively low Zr–Hf contents in the primitive mantle-normalized trace element patterns (Fig. 4) likely suggest the presence of residual zircon in the source region. Additionally, the strongly negative Eu anomalies in the chondrite-normalized REE patterns (Fig. 3) also indicate the presence of residual plagioclase.

Combining the geochronological data (Table 1) with the trace element and Sr–Nd isotope data (Fig. 5 and 7) suggest a two-stage process for the formation of the leucogranite magmas in which (1) an LH derived fluid metasomatises the HH crust subsequent to the India-Asia collision at ~55 Ma, and then (2) the metasomatised source region melts to form the leucogranite magmas during the period 25–9 Ma, which could be more than 10–20 Myr after the original fluid infiltration (for more details see Section 7). Thus it is likely that melting of the metasomatised source region of the Himalayan leucogranites occurs under fluid-absent conditions (Harris and Inger, 1992). On this basis we used a fluid-absent melting model to simulate the trace element concentrations of the leucogranites. To model partial melting of a two-component mixed source region involving a fluid derived from the LH sequence and the bulk HH sequence, we estimated the trace element concentrations in a fluid derived from a pelitic slate (Rashid, 2002; Richards et al., 2005) within the LH (Lesser Himalaya Sequence) to represent those in the LH end-member and chose the trace element concentrations in a biotite paragneiss (Inger and Harris, 1993; Richards et al., 2005) from the High Himalayan Crystalline Series to approximate the HH end-member (Fig. 7). The two-component mixed source of the leucogranites is likely formed of enriched domains of biotite paragneiss within the HH sequence, metasomatised by a fluid derived by

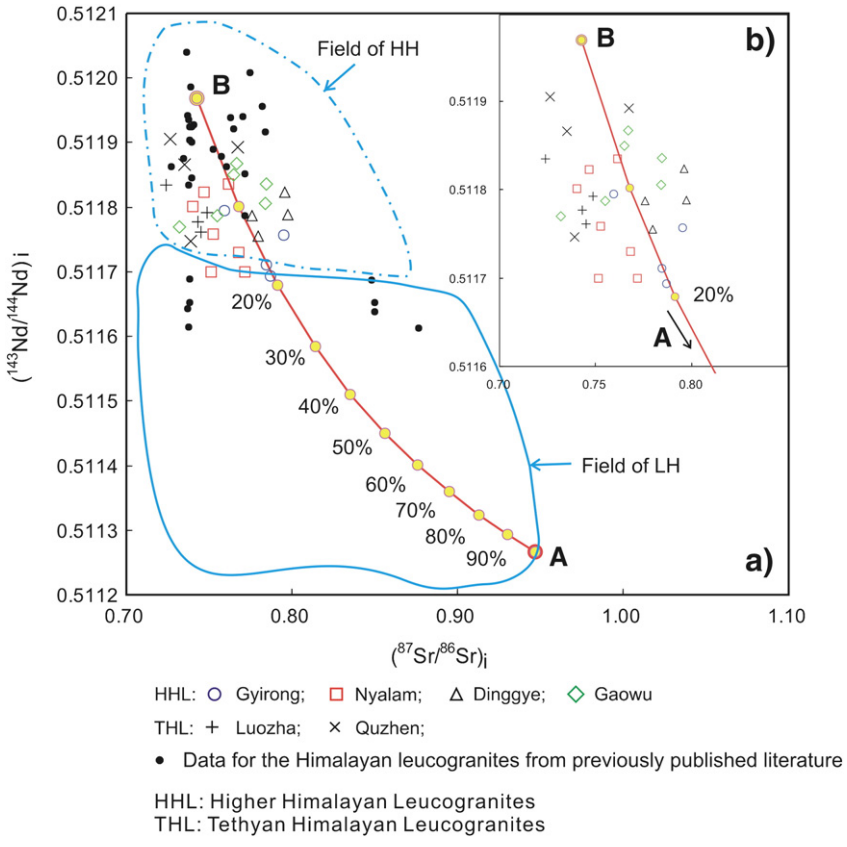

Fig. 5. (a) $(^{143}Nd/^{144}Nd)_i$ vs $(^{87}Sr/^{86}Sr)_i$. Abbreviations are as follows (for more details see the main text): LH (Lesser Himalaya Sequence), HH (Higher Himalayan Crystalline Sequence). Fields for LH and HH metasediments are from King et al. (2011), age corrected to 10 Ma. Filled black circles represent data for Himalayan leucogranites from previously published literature (Deniel et al., 1987; Inger and Harris, 1993; Searle et al., 1997; Harrison et al., 1999; Zhang et al., 2004, 2005; Liao et al., 2006; King et al., 2011). $(^{87}Sr/^{86}Sr)_i$ and $(^{143}Nd/^{144}Nd)_i$ data for the HHL and THL are both age-corrected to 10 Ma (age of the Himalayan leucogranites studied as King et al. (2011) indicated). The red continuous line labeled with filled yellow circles indicates a simple two-component mixing curve between end-members A and B. A is a fluid derived from pelitic slates (W64; Richards et al., 2005) within the LH sequence and B is a biotite gneiss (W41; Richards et al., 2005) from the HH (High Himalayan Crystalline Series). The numbers (%) shown on the filled yellow circles on the red curve denote the proportions of fluid derived from the LH (Lesser Himalaya Sequence) in the source region of the Himalayan leucogranites. The detailed calculation procedures are explained in the text and Table 6. (b) An enlarged view of the Sr–Nd isotope data for the leucogranites in (a).

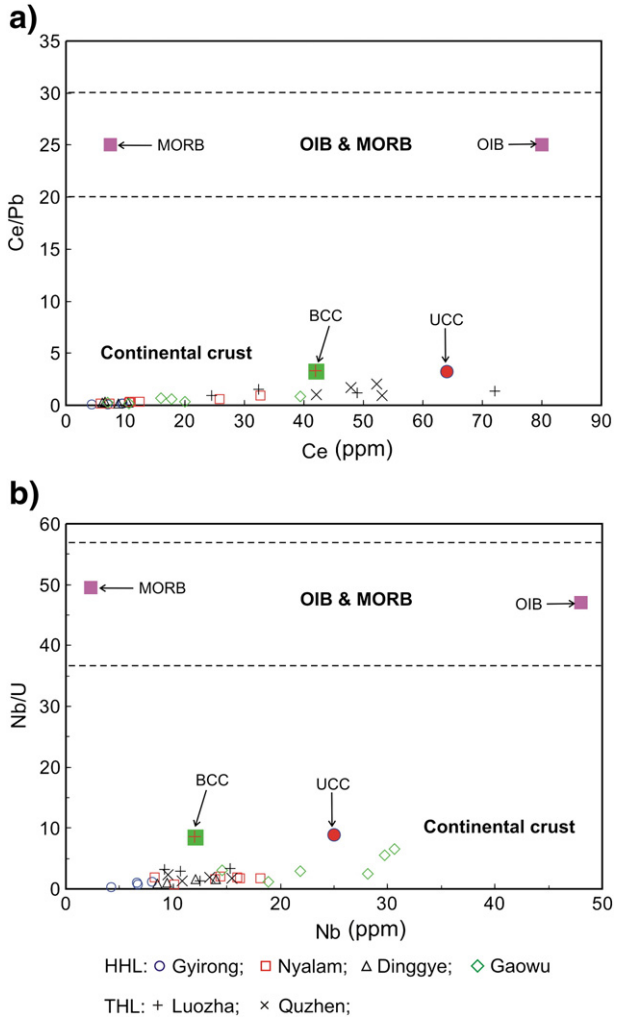

Fig. 6. (a) Ce/Pb vs Ce (ppm); (b) Nb/U vs Nb (ppm). Data for MORB and OIB are taken from Sun and McDonough (1989). Data for UCC (Upper Continental Crust) and BCC (Bulk Continental Crust) are from Taylor and McLennan (1985) and Rudnick and Fountain (1995), respectively. OIB & MORB: field for OIB and MORB; Continental crust: field for continental crust.

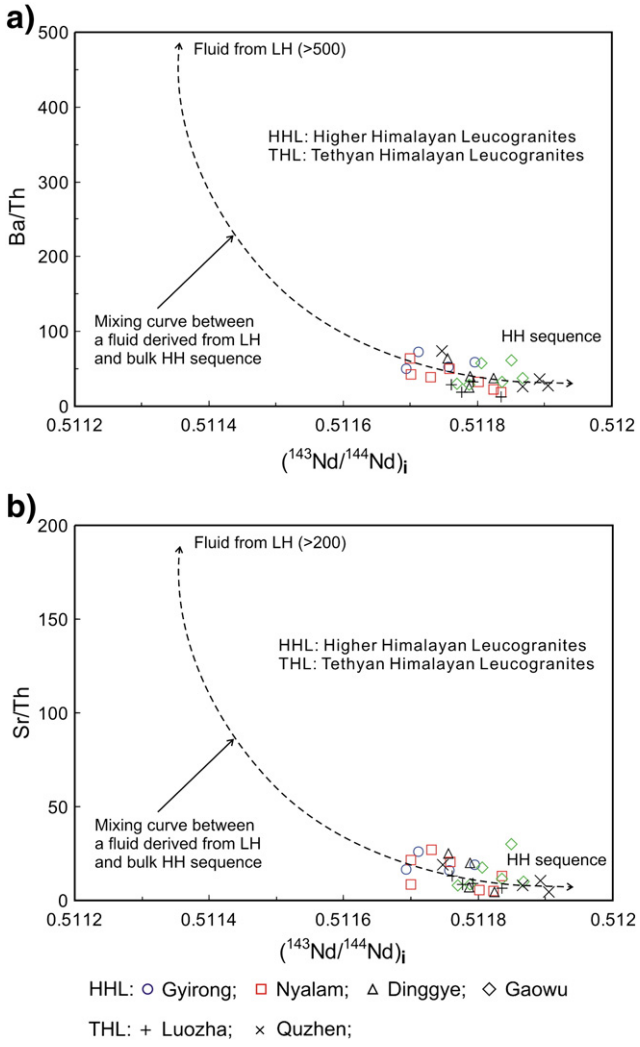

Fig. 7. (a) Ba/Th vs $(^{143}Nd/^{144}Nd)_i$; (b) Sr/Th vs $(^{143}Nd/^{144}Nd)_i$. The dashed line represents a purely schematic mixing curve between a fluid derived from the LH (Lesser Himalaya) sequence and the bulk HH (High Himalayan Crystalline) sequence. Ba/Th and Sr/Th value fields are calculated using the method of Tatsumi and Hanyu (2003) based on the compositions of bulk LH pelitic slates (Table 5).

dehydration of pelitic slates in the LH sequence. The biotite paragneiss within the HH sequence is likely to be more easily melted with respect to other lithologies in the HH sequence (Richards et al., 2005). The calculated trace element concentrations in the fluid indicate that most trace elements (e.g. Rb, Ba, U, Sr, K, Pb and La) have higher concentrations than in the bulk pelitic slate (Table 8).

Based on the trace element characteristics of the leucogranites (Figs. 3 and 4), experimental studies (e.g. Patino Douce and Harris, 1998; Koester et al., 2002) and petrogenetic simulations (e.g. Harris and Inger, 1992; Harris et al., 1993; Kawakami and Kobayashi, 2006), we constrained the original mineral assemblage in the two-component mixed source region to be: garnet + zircon + plagioclase + K-feldspar + biotite + allanite. Because we do not know the proportions of these phases precisely, we performed a series of iterative calculations, following the approach of Guo et al. (2005, 2006, 2007), progressively changing the proportions of each mineral phase from 0% to 80% until we obtained the best fit to the primitive mantle-normalized trace element patterns of the leucogranites (Fig. 4). We assumed the following mineral melting mode (the proportion of the mineral phases entering the melt): garnet (−0.25), zircon (0.01), plagioclase (0.24), K-feldspar (0.45), biotite (0.50–0.55) and allanite (0.05), based on previous experimental and simulation studies (e.g. Vielzeuf and Holloway, 1988; Harris and Inger, 1992; Harris et al., 1993; Gardien et al., 1995; Patino Douce and Harris, 1998; Yang et al., 2001; Koester et al., 2002) and the modeling approach of Guo et al. (2005, 2006, 2007). The mineral-melt trace element partition coefficients (Table 7) used in the calculations were taken from Harris and Inger (1992) and the GERM database (Geochemical Earth Reference Model; http://www.earthref.org/). Details of the calculation method for the trace element modeling are given in Guo et al. (2005, 2006, 2007).

The results of the calculations suggest that the original mineral proportions in the mixed source region could have been different during the generation of the Tg (tourmaline leucogranites) and the 2 mg (two-mica leucogranites); the modal source mineralogy for Tg

Table 5
Ba/Th and Sr/Th in the HH and LH sequences and the leucogranites.

	The HH sequence	The LH sequence	Leucogranites
Ba/Th	8.65–93.22 (n = 18)	16.99–59.55 (n = 20)	12.32–74.44 (n = 29)
Sr/Th	1.55–26.50 (n = 18)	0.85–8.21 (n = 20)	4.39–30.11 (n = 29)

Ba/Th and Sr/Th in the HH and LH sequences are from data published in : Deniel et al., 1987; Harris and Inger, 1992; Harris et al., 1993; Inger and Harris, 1993; Ahmad et al., 2000; Miller et al., 2001; Rashid, 2002; Richards et al., 2005.
Ba/Th and Sr/Th in the leucograbites are calculated from the data in Table 3.

Table 6
Sr–Nd isotope two-component mixing model calculation results.

LH-derived fluid (%)	0%	10%	20%	30%	40%	50%	60%
$(^{87}Sr/^{86}Sr)_M$	0.742835	0.767666	0.791333	0.813915	0.835487	0.856114	0.875857
$(^{143}Nd/^{144}Nd)_M$	0.511969	0.511802	0.511679	0.511585	0.511511	0.511451	0.511401

$(^{87}Sr/^{86}Sr)_M$ and $(^{143}Nd/^{144}Nd)_M$ are the initial Sr and Nd isotopic compositions of the mixed source calculated by the two-component mixing model.
LH-derived fluid (%) is the proportion of a fluid derived from the LH (Lesser Himalaya) sequence in the source region of the Himalayan leucogranites.
The expression of Sr–Nd isotope two-component mixing model follows that of Faure and Mensing (2005).
Based on previous studies (Ahmad et al., 2000; Richards et al., 2005), we consider a fluid derived from pelitic slates within the LH sequence and a bulk biotite gneiss within the Higher Himalayan (HH) sequence to represent the compositions of the two mixing end-members. The composition of two end-members is as follows (Richards et al., 2005):
A fluid derived from pelitic slate within the LH sequence: $(^{87}Sr/^{86}Sr)_i = 0.947035$; $(^{143}Nd/^{144}Nd)_i = 0.511266$;
The bulk biotite gneiss within the HH sequence: Sr = 122.0 ppm; $(^{87}Sr/^{86}Sr)_i = 0.742835$; Nd = 29.7 ppm; $(^{143}Nd/^{144}Nd)_i = 0.511969$.
$(^{87}Sr/^{86}Sr)_i$ and $(^{143}Nd/^{144}Nd)_i$ data are both age-corrected to 10 Ma in order to compare to those of the Himalayan leucogranites.
The Sr and Nd concentrations in the fluid derived from the LH sequence are as follows:
Mobility for Sr and Nd in sediment-derived fluid is 11% and 3%, respectively, during pelite dehydration processes (Aizawa et al., 1999). H_2O content in the pelitic slate within the LH sequence is 1–3 wt.% based on the data of Richards et al. (2005). Sr concentration is 42.3 ppm and Nd concentration is 41.7 ppm in the pelitic slate within the LH sequence (Richards et al., 2005). Following the calculation method of Tatsumi and Hanyu (2003), we estimated the Sr and Nd concentrations are 152.0 ppm and 83.4 ppm in the fluid derived from the pelitic slate within the LH sequence, respectively.
Abbreviations are as follows (for more details see the main text):
HH: Higher Himalayan sequence;
LH : Lesser Himalayan sequence.

generation involves zircon (0.020–0.035), allanite (0.013–0.015), biotite (0.37–0.52), K-feldspar (0.20–0.21), plagioclase (0.140–0.345) and garnet (0.042–0.080), while that for the 2 mg involves zircon (0.002–0.012), biotite (0.166–0.465), K-feldspar (0.50–0.79), plagioclase (0.002–0.040) and garnet (0.03–0.10). The calculation results confirm no residual allanite in the source region of the 2 mg (two-mica granites) and that the amount of residual garnet is higher in the source region of the THL (0.07–0.10) than that of the HHL (0.03–0.08) (Figs. 4 and 8). The calculated results for the residual mineral proportions confirm the earlier inferences based on the low REE concentrations in the Tg and Fig. 8. Our trace element modeling calculation results indicate that the best-fit modal source mineralogy, including biotite and plagioclase, is consistent with the equilibrium (biotite + plagioclase + quartz = sillimanite + Kfeldspar + melt) under fluid-absent conditions considered in previous studies (e.g., Harris and Inger, 1992). This confirms the fluid-absent melting process.

The best fit model results suggest that a melt with trace element characteristics similar to those of the leucogranites could be generated by 11–16% (Tg) and 7–10% (2 mg) melting of a two-component mixed source region involving 10–17% (Tg) and 3–11% (2 mg) of the fluid derived from the LH sequence in the source region (Table 8 and Fig. 4). The amounts of the fluid derived from the pelitic slate within the LH sequence in the source region of the HHL (including Tg and 2 mg) are 8–17%, whereas those of the THL (almost all 2 mg) are 3–10% (Fig. 4). The amounts of the fluid derived from the pelitic slate within the LH sequence in the source region increases from north (THL) to south (HHL) (Fig. 1).

The preferred calculation results fit the trace element data for the leucogranites extremely well (Fig. 4), and are consistent with the results of the Sr–Nd isotope modeling (Fig. 5 and Table 4). They strongly suggest that the two dominant factors controlling the compositional variations of the HHL and THL (Figs. 2–5) are the relative proportions of the fluid derived from the LH sequence in the source region and the degree of melting of the source.

It should be noted that the modeling results (Table 7 and Fig. 4) depend on assumptions about the initial parameters (e.g. partition coefficients and proportions of melting mineral phases). However, sensitivity calculations indicate that the effect of relative changes in these parameters (i.e. partition coefficients and the proportions in which mineral phases enter the melt) on the final results of the trace element modeling is not significant; this is 1–5% for the trace elements shown in Fig. 4. The variation trends of Fig. 4 are similar when these initial parameters are changed significantly. This indicates that our model calculations are relatively insensitive to the values we assume.

7. A new geodynamic model for the evolution of Himalayan orogen

The modeling results (Figs. 4 and 5) showing increasing amounts of fluid derived from the LH sequence in the two-component mixed source region from north (THL) to south (HHL) may be explained by northward underthrusting of the Indian continent following the onset of the India-Asia collision (~55 Ma) (Fig. 9a). The consistent ages of the leucogranites from south (HHL) to north (THL) indicate that the cause of the melting of the metasomatised crustal source region of the leucogranites cannot easily be attributed to the progressive northward underthrusting of the Indian continent, although this could result in two-component mixing in the source region between the HH sequence and a fluid derived from the underlying LH sequence. If the melting of the metasomatised source region of the leucogranites was directly caused by the northward underthrusting of the Indian continent, it would result in decreasing ages of the resultant leucogranites from south to north, rather than the rather consistent ages observed for the HHL and THL (Table 1). Moreover, the ages of the resultant leucogranites might be expected to be same as that of the onset of northward underthrusting of the Indian continent (i.e. ~55 Ma).

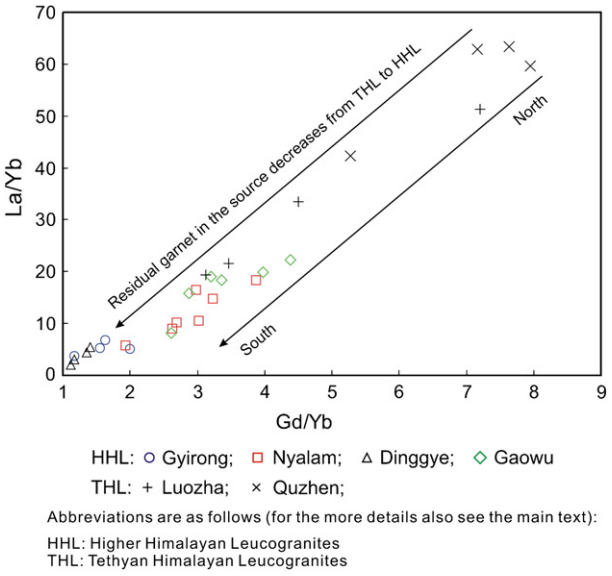

Fig. 8. Variation of La/Yb vs Gd/Yb for the Himalayan leucogranites from this study. Decreasing residual garnet in the source from THL (North) to HHL (South) is explained in details in the text.

Table 7
Mineral-melt partition coefficients for trace element model calculations.

Mineral	Rb	Ba	Th	U	Nb	Ta	K	La	Ce	Pb	Sr
Zircon	0.01	0.01	8.00	37.00	1.70	9.00	0.11	0.09	0.40	1.20	0.01
Allanite	0.19		648.00	11.90	1.70	1.90		2362.00	2063.00	0.92	1.80
Biotite	3.20	5.35	2.00	0.26	4.60	1.20	1.01	15.10	11.00	0.04	7.20
K-feldspar	0.38	3.77	0.30	0.02	0.27	0.49	1.49	1.01	0.86	1.46	0.77
Plagioclase	0.06	13.25	0.11	0.71	0.04	0.13	0.07	4.61	3.87	0.77	1.25
Garnet	0.01	0.02	0.34	0.03	0.01	0.22	0.02	0.001	0.01	0.02	0.02

Mineral	P	Nd	Sm	Zr	Hf	Eu	Ti	Tb	Y	Yb	Lu
Zircon	0.05	0.26	2.00	198.00	140.00	0.45	1.40		6.40		13.00
Allanite		1400.00	756.00	0.29	28.00	122.00		235	95.5	24.50	22.00
Biotite		5.70	4.30	1.80	2.10	0.05	13.60	0.18	2.40	0.12	0.20
K-feldspar	1.16	0.51	0.42	0.21	0.05	2.32		0.01	0.50	0.01	0.01
Plagioclase	0.43	2.56	1.45	0.36	0.29	2.99	0.08	0.02	0.78	0.01	0.01
Garnet	0.18	0.73	6.40	0.40	3.30	11.15	5.60	7.20	9.10	26.90	24.60

Blank denotes no data are available.
Data sources: Harris and Inger (1992); GERM (Geochemical Earth Reference Model) home page, http://www.earthref.org/.

We propose that the underthrusting of the Indian continent following the India-Asia collision (~55 Ma) resulted in the generation of a dehydration fluid from pelitic slates in the LH sequence which metasomatised the overlying HH gneisses (Fig. 7 and Fig. 9a), forming low melting-point domains within the HH gneisses that were easily melted during subsequent phases of uplift and decompression (and/or re-heating), resulting in the generation of the leucogranite magmas. This suggests that the leucogranite magmatism may signal important phases of decompression and/or re-heating of the lithosphere between 25 and 9 Ma in the Himalayan orogen.

The convergence rate between India and Asia abruptly decreased during the period ~23 Ma–9 Ma (Lee and Lawver, 1995). This may have led to extension in the Himalayas since the early Miocene as a consequence of lithospheric flexural bending in response to steepening of the subducted slab of Indian lithosphere. Previous studies (e.g. Replumaz et al., 2004; King et al., 2011) have suggested steepening of the northward subducting Indian slab since the early Miocene. Such a steepening of the subducted Indian slab could have caused re-heating of the lithosphere of the Himalayan orogen related to upwelling of hotter asthenospheric mantle.

Previous studies (e.g. Guillot et al., 1994; Carosi et al., 1998; Xu et al., 2006) have indicated that the South Tibetan Detachment (STD) system is a huge Late Oligocene–Miocene (25–12 Ma) N–S extension-induced normal fault juxtaposing the TH sequence in the hanging wall against the HH sequence in the footwall (Fig. 9b). The HHL are located within the STD system along a near east–west striking trend (Figs. 1 and 9b), and there are consistent ages between the HHL and movement on the STD system (Table 1). The North Himalayan Antiform (NHA; Fig. 1) is also thought to be a N–S extensional feature formed during this period (Zhang et al., 2004, 2005; Aoya et al., 2005), possibly related to flexural bending of the lithosphere due to slab steepening (King et al., 2011). The THL were emplaced along the NHA and have similar ages to the

Table 8
The best-fit results of the trace element modeling.

Body name	Rock type	Melting (%)	LH fluid in source (%)	Rb	Ba	Th	U	Nb	Ta	K_2O	La	Ce	Pb	Sr
LH-derived fluid				174.80	2204.00	20.50	7.40	17.36	0.00	18.40	72.28	105.17	495.73	152.00
Gyirong	Tg	14	17	191.51	133.75	4.60	3.58	7.99	0.89	3.28	1.94	3.98	55.33	47.87
Nyalam	Tg	11	16	181.38	137.80	3.96	3.61	7.44	0.88	2.98	1.68	3.44	53.08	45.33
Nyalam	2 mg	9	10	164.97	187.39	28.25	7.64	6.80	0.93	2.09	7.89	18.79	31.30	44.48
Dinggye	Tg	14	13	172.87	130.54	5.70	2.74	6.92	0.80	2.68	2.28	4.79	45.60	43.48
Dinggye	2 mg	10	11	144.17	202.35	26.79	17.46	5.97	0.93	1.91	7.08	16.92	33.28	39.47
Gaowu	Tg	16	10	140.54	168.57	4.89	2.48	5.46	0.70	2.02	1.95	4.16	41.39	37.21
Gaowu	2 mg	9	8	308.14	215.30	44.82	7.63	14.67	1.13	2.94	18.38	42.41	22.97	89.48
Luozha	2 mg	7	10	304.90	226.18	44.08	7.85	14.41	1.13	3.10	17.64	40.71	26.45	87.29
Quzhen	2 mg	10	3	292.90	208.51	42.23	7.14	12.91	1.19	2.57	16.13	38.22	18.39	82.94

Body name	Rock type	Melting (%)	LH fluid in source (%)	P_2O_5	Nd	Sm	Zr	Hf	Eu	TiO_2	Tb	Y	Yb	Lu
LH-derived fluid				0.03	83.40	2.34	71.00	0.00	0.40	1.42	1.44	54.60	6.00	1.02
Gyirong	Tg	14	17	0.15	3.20	0.84	48.55	1.61	0.29	0.13	0.17	12.38	0.86	0.14
Nyalam	Tg	11	16	0.15	2.74	0.74	48.07	1.56	0.27	0.12	0.14	10.88	0.69	0.11
Nyalam	2 mg	9	10	0.13	17.11	3.32	87.76	2.93	0.51	0.11	0.55	17.62	0.95	0.16
Dinggye	Tg	14	13	0.15	3.79	1.04	34.58	1.25	0.32	0.11	0.19	12.61	0.88	0.13
Dinggye	2 mg	10	11	0.12	15.80	3.19	201.75	5.28	0.64	0.10	0.67	18.64	1.24	0.21
Gaowu	Tg	16	10	0.13	3.22	0.91	30.34	1.09	0.31	0.08	0.14	9.99	0.55	0.09
Gaowu	2 mg	9	8	0.15	35.97	6.28	88.65	3.39	0.44	0.29	0.70	25.74	1.24	0.20
Luozha	2 mg	7	10	0.15	34.80	5.16	85.74	3.10	0.39	0.26	0.51	20.95	0.81	0.13
Quzhen	2 mg	10	3	0.16	30.09	4.55	90.65	3.15	0.37	0.20	0.28	16.25	0.48	0.08

Contents of the elements are in ppm; K_2O, P_2O_5 and TiO_2 in wt.%.
For more detailed discussions for the model calculation see the main text.
The trace element concentrations in the fluid derived from the LH sequence are calculated following the method described in Table 6.
The expression and approach of the non-modal batch partial melting model follow that of Guo et al. (2005, 2006, 2007).
Abbreviations are as follows (for more details see the main text):
LH: Lesser Himalayan sequence; Tg: tourmaline leucogranites; 2 mg: two-mica leucogranites.

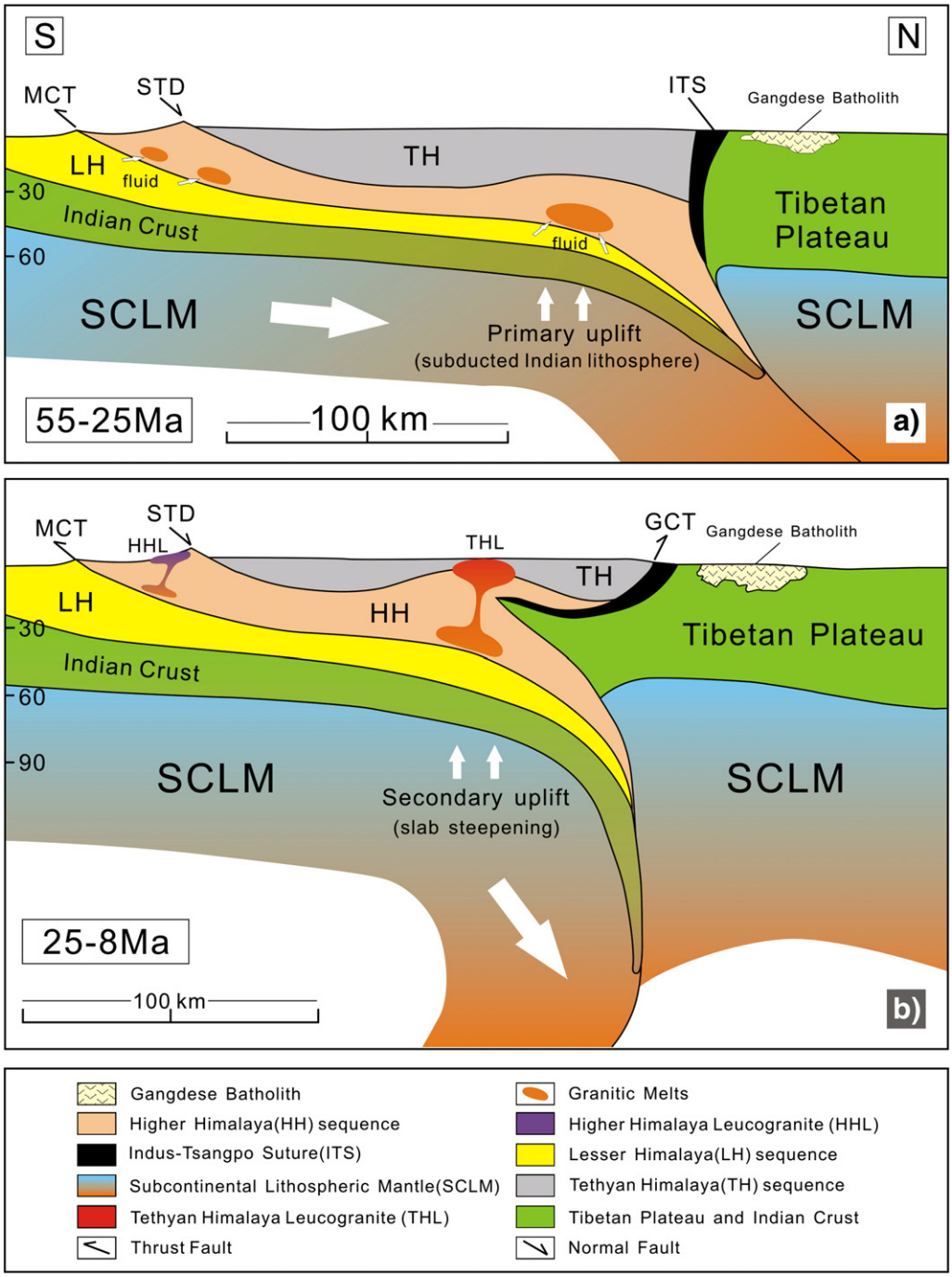

Fig. 9. Petrogenetic model for the Himalayan leucogranites. The diagram shows an N–S cross section. (a) Northward underthrusting of the LH (Lesser Himalayan Sequence) beneath the HH (High Himalayan Crystalline Series) along the MCT (Main Central Thrust) causes compressional deformation in the Himalayas and the generation of low melting-point metasomatised domains which result from enrichment by fluids derived from dehydration of pelitic slates within the LH (Lesser Himalayan Sequence) during India-Asia collision from ~55 Ma to 25 Ma. The northward underthrusting of the Indian continental lithosphere leads to primary uplift of the Himalayas since the onset of India–Asia collision. (b) The metasomatised domains undergo decompressional partial melting because of tectonic extension as a response to Indian slab steepening, resulting in the generation of the Himalayan leucogranite magmas during the period 25 Ma–8 Ma. The Indian plate flexural response to the slab steepening results in the secondary uplift of the Himalayas during this period. (a) and (b) are modified after King et al. (2011).

formation of the NHA (Figs. 1 and 9b; Table 1). This suggests that both the STD and the NHA were closely associated with extension-related decompression melting of low melting-point metasomatised domains within the HH gneisses, previously enriched by a fluid derived from the LH sequence, resulting in the generation of the Himalayan leucogranites during the period 9–25 Ma (Table 1 and Fig. 9b). The Himalayan leucogranites are older than ~9 Ma (Table 1), suggesting cessation of N-S extension by ~9 Ma. This is supported by significant uplift after ~7 Ma of the HH sequence (Wang et al., 2006). The data suggest that the leucogranites may provide a petrologic record of the Late Oligocene–Miocene N–S extension of the Himalayan–Tibetan orogen.

King et al. (2011), in a detailed field and geochemical study of the Sakya basement dome (Number 24, Fig. 1) within the THS, have identified two groups of granitic intrusions that have distinct field relationships, geochemistry, ages and tectonic setting. The older group, which they term “anastomosing equigranular leucogranites”, was emplaced between 28 and 23 Ma and is considered to have been generated by anatexis of the granite gneisses that form the core of the

dome. These leucogranites are characterized by high HREE/LREE ratios and Y contents, which King et al. (2011) relate to melting under conditions of high fluid phase activity involving biotite in the melting reaction. A younger group of leucogranites, termed by these authors "Discrete Porphyritic Plutons", was emplaced between 15 and 9 Ma and considered to be derived by decompression-induced, fluid-absent melting of a metasedimentary source. We do not see such a distinction in our data set between older and younger leucogranites; this may, however, reflect the much better geochronological control in the study of King et al. (2011). All of our samples are, however, both geochemically and in terms of field relationships, similar to the Discrete Porphyritic Plutons of King et al. (2011). Further geochronological studies may be required to refine the ages of some of the older leucogranites in our data set (e.g. Gaowu).

8. Conclusions

This study has identified the role of a two-component mixed source region in the petrogenesis of the Himalayan leucogranites based on Sr–Nd isotope and trace element data. We estimate the relative proportions of the HH sequence (>80%) and a fluid derived from the LH sequence (<20%) in the metasomatised source region using trace element and isotope modeling calculations. We propose that northward underthrusting of the Indian continent resulted in the release of a LH-derived dehydration fluid that metasomatised the overlying HH gneisses, forming low melting-point enriched domains in the HH crustal source region. Lithospheric extension in Late Oligocene–Miocene times (26–9 Ma) resulted in decompression melting of these metasomatised domains, generating the Late Oligocene–Miocene Himalayan leucogranites; this extension is linked to steepening of the subducted Indian slab. The differences in the proportion of fluid derived from the LH sequence in the source region, together with the variable degrees of partial melting of the source, resulted in the variations in the major element, trace element and Sr–Nd isotope compositions of the HHL (in the south) and THL (in the north). The proportion of the fluid derived from the LH sequence in the source region of the HHL (5–19%) was higher than that in the source of the THL (2–13%). The HHL resulted from 9 to 16% melting; THL resulted from 7 to 10% melting.

Acknowledgments

This study was supported by a joint project between the Royal Society of London and National Natural Science Foundation of China (NSFC), by a grant from Chinese Academy of Sciences (KZCX2-YW-Q09-05), and by grants from the NSFC (Nos.: 41020124002 and 40773023). We are grateful to Professors Yaoling Niu and Jiaqi Liu, and Drs. Z. Liao, Y. Di, Y. Lu, X. Chen, D. Jiang, M. Zhang, W. Guo and F. Meng for their help. We thank the reviewers for their constructive comments, which have greatly improved an earlier version of the manuscript.

References

Ahmad, T., Harris, N., Bickle, M., Chapman, H., Bunbury, J., Prince, C., 2000. Isotopic constraints on the structural relationships between the Lesser Himalayan Series and the High Himalayan Crystalline Series, Garhwal Himalaya. Geological Society of America Bulletin 112, 467–477.

Aizawa, Y., Tatsumi, Y., Yamada, H., 1999. Element transport during dehydration of subducting sediments: implication for arc and ocean island magmatism. Island Arc 8, 38–46.

Aoya, M., Wallis, S.R., Terada, K., Lee, J., Kawakami, T., Wang, Y., Heizler, M., 2005. North–south extension in the Tibetan crust triggered by granite emplacement. Geology 33, 853–856.

Barbarin, B., 1999. A review of the relationships between granitoid types, their origins and their geodynamic environments. Lithos 46, 605–626.

Bird, P., 1978. Initiation of intracontinental subduction in the Himalaya. Journal of Geophysical Research 83, 4975–4987.

Carosi, R., Lombardo, B., Molli, G., Musumeci, G., Pertusati, P.C., 1998. The south Tibetan detachment system in the Rongbuk valley, Everest region. Deformation features and geological implications. Journal of Asian Earth Sciences 16, 299–311.

Davidson, C., Grujic, D.E., Hollister, L.S., Schmid, S.M., 1997. Metamorphic reactions related to decompression and synkinematic intrusion of leucogranite, High Himalayan Crystallines, Bhutan. Journal of Metamorphic Geology 15, 593–612.

Deniel, C., Vidal, P., Fernandez, A., Le Fort, P., Peucat, J.J., 1987. Isotopic study of the Manaslu granite (Himalaya, Nepal): inferences on the age and source of Himalayan leucogranites. Contributions to Mineralogy and Petrology 96, 78–92.

DePaolo, D.J., 1988. Neodymium Isotope Geochemistry: An Introduction. Springer Verlag, New York. 230pp.

Dèzes, P.J., Vannay, J.-C., Steck, A., Bussy, F., Cosca, M., 1999. Synorogenic extension: quantitative constraints on the age and displacement of the Zanskar shear zone (northwest Himalaya). Geological Society of America Bulletin 111, 364–374.

Edwards, M.A., Harrison, T.M., 1997. When did the roof collapse? Late Miocene north–south extension in the High Himalaya revealed by Th–Pb monazite dating of the Khula Kangri granite. Geology 25, 543–546.

Elburg, M.A., van Bergen, M., Hoogewerff, J., Foden, J., Vroon, P., Zulkarnain, I., Nasution, A., 2002. Geochemical trends across an arc-continent collision zone: magma sources and slab-wedge transfer processes below the Pantar Strait volcanoes, Indonesia. Geochimica et Cosmochimica Acta 66, 2771–2789.

Faure, G., Mensing, T.M., 2005. Isotopes: Principles and Applications (third edition). John Willey & Sons, Inc, Hoboken, New Jersey, pp. 347–362.

Frost, B.R., Barnes, C.G., Collins, W.J., Arculus, R.J., Ellis, D.J., Frost, C.D., 2001. A geochemical classification for granitic rocks. Journal of Petrology 42, 2033–2048.

Gardien, V., Thompson, A.B., Grujic, D., Ulmer, P., 1995. Experimental melting of biotite + plagioclase + quartz ± muscovite assemblages and implications for crustal melting. Journal of Geophysical Research 100, 15581–15591.

Godin, L., Parrish, R.R., Brown, R.L., Hodges, K.V., 2001. Crustal thickening leading to exhumation of the Himalayan metamorphic core of central Nepal: insight from U–Pb geochronology and $^{40}Ar/^{39}Ar$ thermochronology. Tectonics 20, 729–747.

Goldstein, S.L., O'Nions, R.K., Hamilton, P.J., 1984. A Sm–Nd isotopic study of atmospheric dusts and particulates from major river systems. Earth and Planetary Science Letters 70, 221–236.

Guillot, S., Hodges, K.V., Le Fort, P., Pêcher, A., 1994. New constraints on the age of the Manaslu leucogranite: evidence for episodic tectonic denudation in the Central Himalayas. Geology 22, 559–562.

Guillot, S., Le Fort, P., 1995. Geochemical constraints on the bimodal origin of High Himalayan leucogranites. Lithos 35, 221–234.

Guo, Z., Hertogen, J., Liu, J., Pasteels, P., Boven, A., Punzalan, L., He, H., Luo, X., Zhang, W., 2005. Potassic magmatism in western Sichun and Yunnan provinces, SE Tibet, China: petrological and geochemical constraints on petrogenesis. Journal of Petrology 46, 33–78.

Guo, Z., Wilson, M., Liu, J., 2007. Post-collisional adakites in south Tibet: products of partial melting of subduction-modified lower crust. Lithos 96, 205–224.

Guo, Z., Wilson, M., Liu, J., Mao, Q., 2006. Post-collisional, potassic and ultrapotassic magmatism of the northern Tibetan Plateau: constraints on characteristics of the mantle source, geodynamic setting and uplift mechanisms. Journal of Petrology 47, 1177–1220.

Harris, N., Inger, S., Massey, J., 1993. The role of fluids in the formation of High Himalayan leucogranites. In: Treloar, P.J., Searle, M.P. (Eds.), Himalayan Tectonics: Geological Society of London Special Publications, 74, pp. 391–400.

Harris, N., Massey, J., 1994. Decompression and anatexis of Himalayan metapelites. Tectonics 13, 1537–1546.

Harris, N.B.W., Inger, S., 1992. Trace element modelling of pelite-derived granites. Contributions to Mineralogy and Petrology 110, 46–56.

Harrison, T.M., Grove, M., McKeegan, K.D., Coath, C.D., Lovera, O.M., Le Fort, P., 1999. Origin and episodic emplacement of the Manaslu intrusive complex, central Himalaya. Journal of Petrology 40, 3–19.

Harrison, T.M., Lovera, O.M., Grove, M., 1997. New insights into the origin of two contrasting Himalayan granite belts. Geology 25, 899–902.

Harrison, T.M., McKeegan, K.D., Le Fort, P., 1995. Detection of inherited monazite in the Manaslu leucogranite by $^{208}Pb/^{232}Th$ ion microprobe dating: crystallization age and tectonic implications. Earth and Planetary Science Letters 133, 271–282.

Hawkesworth, C.J., Turner, S.P., McDermott, F., Peate, D.W., van Calsteren, P., 1997. U–Th isotopes in arc magmas: implications for element transfer from the subducted crust. Science 276, 551–555.

Hodges, K.V., Parrish, R.R., Searle, M.P., 1996. Tectonic evolution of the central Annapurna Range, Nepalese Himalayas. Tectonics 15, 1264–1291.

Hofmann, A.W., Jochum, K.P., Seufert, M., White, W.M., 1986. Nb and Pb in oceanic basalts: new constraints on mantle evolution. Earth and Planetary Science Letters 79, 33–45.

Inger, S., Harris, N., 1993. Geochemical constraints on leucogranite magmatism in the Langtang valley, Nepal Himalaya. Journal of Petrology 34, 345–368.

Jacobsen, S.B., Wasserburg, G.J., 1980. Sm–Nd isotopic evolution of chondrites. Earth and Planetary Science Letters 50, 139–155.

Johnson, A.C., Plank, T., 1999. Dehydration and melting experiments constration the fate of subducted sediments. Geochemistry Geophysics Geosystems 1 Paper number 1999GC000014.

Kawakami, T., Aoya, M., Wallis, S.R., Lee, J., Terada, K., Wang, Y., Heizler, M., 2007. Contact metamorphism in the Malashan dome, North Himalayan gneiss domes, southern Tibet: an example of shallow extensional tectonics in the Tethys Himalaya. Journal of Metamorphic Geology 25 (8), 831–853.

Kawakami, T., Kobayashi, T., 2006. Trace element composition and degree of partial melting of pelitic migmatites from the Aoyama area, Ryoke metamorphic belt, SW Japan: implications for the source region of tourmaline leucogranites. Gondwana Research 9, 176–188.

King, J., Harris, N., Argles, T., Parrish, R., Zhang, H., 2011. Contribution of crustal anatexis to the tectonic evolution of Indian crust beneath southern Tibet. Geological Society of America Bulletin 123, 218–239.

Koester, E., Pawley, A.R., Fernandes, L.A.D., Porcher, C.C., Soliani Jr., A.E., 2002. Experimental melting of cordierite gneiss and the petrogenesis of syntranscurrent peraluminous granites in southern Brazil. Journal of Petrology 43, 1595–1616.
Kogiso, T., Tatsumi, Y., Nakano, S., 1997. Trace element transport during dehydration processes in the subducted oceanic crust: 1. Experiments and implications for the origin of ocean island basalts. Earth and Planetary Science Letters 148, 193–205.
Lee, J., McClelland, W., Wang, Y., Blythe, A., McWilliams, M., 2006. Oligocene–Miocene middle crustal flow in southern Tibet: geochronology of Mabja dome. In: Law, R.D., Searle, M.P., Godin, L. (Eds.), Channel Flow, Ductile Extrusion and Exhumation of Lower-Mid Crust in Continental Collision Zones: Geological Society of London Special Publication, 268, pp. 445–469.
Lee, J., Whitehouse, M.J., 2007. Onset of mid-crustal extensional flow in southern Tibet: evidence from U/Pb zircon ages. Geology 35 (1), 45–48.
Lee, T.-Y., Lawver, L.A., 1995. Cenozoic plate reconstruction of Southeast Asia. Tectonophysics 251, 85–138.
Le Fort, P., Cuney, M., Deniel, C., France-Lanord, C., Sheppard, S.M.F., Upreti, B.N., Vidal, P., 1987. Crustal generation of the Himalayan leucogranites. Tectonophysics 134, 39–57.
Liao, Z.L., Mo, X.X., Pan, G.T., Zhu, D.C., Wang, L.Q., Jiang, X.S., Zhao, Z.D., 2003. The distribution and tectonic significance of peraluminous granites in southern Xizang. Sedimentary Geology and Tethyan Geology 23, 12–20 (in Chinese with English abstract).
Liao, Z., Mo, X., Pan, G., Zhu, D., Wang, L., Zhao, Z., Geng, Q., Dong, G., 2006. Quzhen peraluminous granite, Tibet: geochemical characteristics and geodynamic significance. Acta Petrologica Sinica 22, 845–854 (in Chinese with English abstract).
Liu, G., Jin, C., Wang, F., Wang, S., Wang, B., Xu, R., Ding, X., 1990. Tectonic Evolution of the Himalayan Lithosphere. Beijing: Geological Publishing House 100–321 (in Chinese with English abstract).
Lugmair, G.W., Marti, K., 1978. Lunar initial $^{143}Nd/^{144}Nd$: differential evolution of the lunar crust and mantle. Earth and Planetary Science Letters 39, 349–357.
Malaski, H., Matte, P., Brunal, M., Xiao, X., 1988. $Argon^{39}$–$argon^{40}$ dating of metamorphic and plutonic events in the north and high Himalaya belts (southern Tibet-China). Tectonics 7 (2), 299–326.
McCulloch, M.T., Black, L.P., 1984. Sm–Nd isotopic systematics of Enderby Land granulites and evidence for the redistribution of Sm and Nd during metamorphism. Earth and Planetary Science Letters 71, 46–58.
Miller, C., Thoni, M., Frank, W., Grasemann, B., Klotzli, U., Guntli, P., Draganits, E., 2001. The early Palaeozoic magmatic event in the Northwest Himalaya, India: source, tectonic setting and age of emplacement. Geological Magazine 138, 237–251.
Murphy, M.A., Harrison, T.M., 1999. Relationship between leucogranites and the Qomolangma detachment in the Rongbuk Valley, south Tibet. Geology 27, 831–834.
Nelson, K.D., Zhao, W., Brown, L.D., Kuo, J., Che, J., Liu, X., Klemperer, S.L., Makovsky, Y., Meissner, R., Mechie, J., Kind, R., Wenzel, F., Ni, J., Nabelek, J., Chen, L., Tan, H., Wei, W., Jones, A.G., Booker, J., Unsworth, M., Kidd, W.S.F., Hauck, M., Alsdorf, D., Ross, A., Cogan, M., Wu, C., Sandvol, E., Edwards, M., 1996. Partially melten middle crust beneath southern Tibet: synthesis of project INDEPTH results. Science 274, 1684–1688.
Noble, S.R., Searle, M.P., 1995. Age of crustal melting and leucogranite formation from U–Pb zircon and monazite dating in the western Himalaya, Zanskar, India. Geology 23, 1135–1138.
Pan, G., Ding, J., 2004. An Introduction of Geological Map of the Tibetan Plateau and Neighbouring Area. Chengdu Map Press, Chengdu. 133pp. (in Chinese).
Patino Douce, A.E., Harris, N., 1998. Experimental constraints on Himalayan anatexis. Journal of Petrology 39, 689–710.
Quigley, M., Liangjun, Y., Xiaohan, L., Wilson, C.J.L., Sandiford, M., Phillips, D., 2006. $^{40}Ar/^{39}Ar$ thermochronology of the Kampa Dome, southern Tibet: implications for tectonic evolution of the North Himalayan gneiss domes. Tectonophysics 421 (3–4), 269–297.
Rashid, S.A., 2002. Geochemical characteristics of Mesoproterozoic clastic sedimentary rocks from the Chakrata Formation, Lesser Himalaya: implications for crustal evolution and weathering history in the Himalaya. Journal of Asian Earth Sciences 21, 283–293.
Replumaz, A., Karason, H., van der Hilst, R.D., Besse, J., Tapponier, P., 2004. 4-D evolution of SE Asia's mantle from geological reconstructions and seismic tomography. Earth and Planetary Science Letters 221, 103–115.
Richards, A., Argles, T., Harris, N., Parrish, R., Ahmad, T., Darbyshire, F., Draganits, E., 2005. Himalayan architecture constrained by isotopic tracers from clastic sediments. Earth and Planetary Science Letters 236, 773–796.
Richards, A., Parrish, R., Harris, N., Argles, T., Zhang, L., 2006. Correlation of lithotectonic units across the eastern Himalaya, Bhutan. Geology 34, 341–344.
Rudnick, R.L., Fountain, D.M., 1995. Nature and composition of the continental crust: a lower crustal perspective. Reviews of Geophysics 33, 267–309.
Scharer, U., 1984. The effect of initial ^{230}Th disequilibrium on young U–Pb ages: the Makalu case, Himalaya. Earth and Planetary Science Letters 67, 191–204.
Scharer, U., Xu, R.H., Allègre, C.J., 1986. U–(Th)–Pb systematics and ages of Himalayan leucogranites, South Tibet. Earth and Planetary Science Letters 77, 35–48.
Searle, M.P., Godin, L., 2003. The South Tibetan Detachment and the Manaslu leucogranite: a structural reinterpretation and restoration of the Annapurna–Manaslu Himalaya, Nepal. Journal of Geology 111, 505–523.
Searle, M.P., Parrish, R.R., Hodges, K.V., Hurford, A., Ayres, M.W., Whitehouse, M.J., 1997. Shisha Pangma leucogranite, South Tibetan Himalaya: field relations, geochemistry, age, origin and emplacement. Journal of Geology 105, 295–317.
Searle, M.P., Simpson, R.L., Law, R.D., Parrish, R.R., Waters, D.J., 2003. The structural geometry, metamorphic and magmatic evolution of the Everest massif, High Himalaya of Nepal-South Tibet. Journal of the Geological Society of London 160, 345–366.
Steiger, R.H., Jager, E., 1977. Subcommission on geochronology: convention on the use of decay constants in geo- and cosmochronology. Earth and Planetary Science Letters 36, 359–362.
Streule, M.J., Searle, M.P., Waters, D.J., Horstwood, M.S.A., 2010. Metamorphism, melting, and channel flow in the Greater Himalayan Sequence and Makalu leucogranite: constraints from thermobarometry, metamorphic modeling, and U–Pb geochronology. Tectonics 29 (5), 1–28.
Sun, S.-S., McDonough, W.F., 1989. Chemical and isotopic systematics of ocean basalts: implications for mantle composition and processes. In: Saunders, A.D., Norry, M.J. (Eds.), Magmatism in the Ocean Basins: Geological Society, London, Special Publications, 42, pp. 313–345.
Sylvester, P.J., 1998. Post-collisional strongly peraluminous granites. Lithos 45, 29–44.
Tatsumi, Y., Hanyu, T., 2003. Geochemical modeling of dehydration and partial melting of subducting lithosphere: toward a comprehensive understanding of high-Mg andesite formation in the Setouchi volcanic belt, SW Japan. Geochemistry Geophysics Geosystems 4 Paper number 2003GC000530.
Taylor, S.R., McLennan, S.M., 1985. The Continental Crust: its Composition and Evolution. Blackwell, Oxford.
Tong, J., Zhong, H., Xia, J., Lu, R., Yang, S., 2003. Geochemical features and tectonic setting of peraluminous granite in the Lhozag area, southern Tibet. Geological Bulletin of China 22, 308–318 (in Chinese with English abstract).
Turner, S., Hawkesworth, C., Rogers, N., Bartlett, J., Worthington, T., Hergt, J., Pearce, J., Smith, I., 1997. ^{238}U–^{230}Th disequilibria, magma petrogenesis, and flux rates beneath the depleted Tonga-Kermadec island arc. Geochimica et Cosmochimica Acta 61, 4855–4884.
Vielzeuf, D., Holloway, J.R., 1988. Experimental determination of the fluid-absent melting relations in the pelitic system. Contributions to Mineralogy and Petrology 98, 257–276.
Visona, D., Lombardo, B., 2002. Two-mica and tourmaline leucogranites from the Everest–Makalu region (Nepal–Tibet): Himalayan leucogranite genesis by isobaric heating? Lithos 62, 125–150.
Wang, Y., Deng, T., Biasatti, D., 2006. Ancient diets indicate significant uplift of southern Tibet after ca. 7 Ma. Geology 34, 309–312.
Wilson, M., 1989. Igneous Petrogenesis: A Global Tectonic Approach. Unwin Hyman, London. 466pp.
Wu, C.D., Nelson, K.D., Wortman, G., Samson, S.D., Yue, Y.J., Li, J.X., Kidd, W.S.F., Edwards, M.A., 1998. Yadong cross structure and South Tibetan Detachment in the east central Himalaya (89°–90°E). Tectonics 17, 28–45.
Xu, Z.Q., Yang, J.S., Qi, X.X., Cui, J.W., Li, H.B., Chen, F.Y., 2006. India–Asia collision: a further discussion of N–S- and E–W-trending detachments and the orogenic mechanism of the modern Himalayas. Geological Bulletin of China 25, 1–14 (in Chinese with English abstract).
Yang, X.S., Jin, Z.M., Huenges, E., Schilling, F.R., Wunder, B., 2001. Experimental study on dehydration melting of natural biotite–plagioclase gneiss from High Himalayas and implications for Himalayan crust anatexis. Chinese Science Bulletin 46, 867–872 (in English).
Yin, A., 2006. Cenozoic tectonic evolution of the Himalayan orogen as constrained by along-strike variation of structural geometry, exhumation history, and foreland sedimentation. Earth Science Reviews 76, 1–131.
Zhang, H.F., Harris, N., Parrish, R., Kelley, S., Zhang, L., Rogers, N., Argles, T., King, J., 2004. Causes and consequences of protracted melting of the mid-crust exposed in the North Himalayan antiform. Earth and Planetary Science Letters 228, 195–212.
Zhang, H.-F., Harris, N., Parrish, R., Zhang, L., Zhao, Z.-D., Li, D.-W., 2005. Geochemistry of North Himalayan leucogranites: regional comparison, petrogenesis and tectonic implications. Earth Science Journal of China University of Geosciences 30, 275–288 (in Chinese with English abstract).